Geomorphology 436 (2023) 108753

Contents lists available at ScienceDirect

Geomorphology

journal homepage: www.journals.elsevier.com/geomorphology

Improving filtering methods based on the Fast Fourier Transform to delineate objective relief domains: An application to Mare Ingenii lunar area

A. González-Díez [a,*], J.A. Barreda-Argüeso [a], L. Rodríguez-Rodríguez [b], M.W. Doughty [a], A.J. Riquelme [c]

[a] Departamento de Ciencias de la Tierra y Física de la Materia Condensada, Universidad de Cantabria, Avda. Los Castros, s/n, 39005 Santander, Spain
[b] Departamento de Geología, Universidad de Oviedo, C. Jesús Arias de Velasco s/n, 33005 Oviedo, Spain
[c] Departamento de Ingeniería Civil, Escuela Politécnica Superior de Alicante, Universidad de Alicante, Crta. San Vicente del Raspeig s/n, 03690, Spain

ARTICLE INFO

Keywords:
Crater depressions
High-pass FFT filtering
Butterworth transference Function
Synthetic relief models
Mare Ingenii crater inventory
Objective relief domains

ABSTRACT

A recent study has proven that high-pass filtering (HPF) based on the Fast Fourier Transform (FFT) is a rapid and efficient computational method for the semi-automated detection of geomorphic features from high-resolution digital elevation models (DEM). Although this new approach shows great potential for cartographic purposes using remote sensing data, some methodological improvements are still required in the following areas: (i) to develop a robust criteria for filter radius selection; (ii) to test the relationship between filter vectors and landscape form, and explore how DEM artefacts (vegetation, anthropic structures, etc.) can interfere with landform detection; and (iii) to explore filter response regarding generalisation and blurring effects when working with landscapes composed of landforms of different scales that are superimposed on one another. These topics are addressed here through two experiments (Experiment_1 and Experiment_2) with synthetic digital relief models inspired in the lunar landscape. Finally, the improved methodology was applied on the Mare Ingenii lunar relief (Experiment_3) using the Lunar Orbiter Laser Altimeter DEM and the results were tested against ground truths (GTs) developed using the extensive database available at Astropedia website and an ad hoc crater map. The analysis of existing frequencies in a 2D DEM signal through the true magnitude-true frequency plot provides an objective method for filter radius selection, and the use of a Butterworth transference function enables a more versatile filtering. Experiment_1 demonstrates a close correspondence between vectors obtained by filtering called Filtered Geomorphic References (FGRs) and the synthetic landform selected. The accuracy indicators from Experiment_1 and 2 show the good results obtained in the correspondence between FGRs and crater depressions, either from flat-bottomed to bowl shapes. Experiments 2 and 3 confirm that in landscapes generated by superimposed geomorphic features of different sizes, the smaller the crater, the better the filters detect its boundaries. Moreover, the spatial repeatability of FGRs can be used as a cartographic criterion in the identification of crater shape depressions or hills. Besides, the criterion is useful to assess true reality mapped in the GT employed. Finally, the objective geomorphic units obtained by combining the FGRs demonstrate their usefulness for the objective characterisation of the moonscape. Using the synthetic landscapes, the FGRs identify those relief domains composed of depressions and hills.

1. Introduction

The application of a High-Pass Filter based on the Fast Fourier Transform (HPF-FFT[1]) constitutes a rapid means for the semi-automated detection of landforms from a high-resolution digital elevation model (DEM) of a relief (González-Díez et al., 2021). The tool showed a successful application in the analysis of a karstic relief characterised by a great diversity of morphologies, sizes (either macro or mesoscale), relief polarity, and displaying a broad variety of altitudes and countless inflection points (González-Díez et al., 2021). An advantage of the method

* Corresponding author.
E-mail address: gonzalea@unican.es (A. González-Díez).

[1] Non-standard acronyms: High-Pass Filter based on the Fast Fourier Transform

https://doi.org/10.1016/j.geomorph.2023.108753
Received 27 April 2022; Received in revised form 23 May 2023; Accepted 24 May 2023
Available online 5 June 2023

is that HPF-FFT is sensitive to slight changes in relief polarity regardless of their topographic location, whether in flat areas, slopes, depressions, or valley bottoms, allowing the detection of geomorphic objective limits and the delineation of Filtered Geomorphic References (FGRs[2]). FGRs separate areas of either positive or negative polarity (i.e., areas above or below the surrounding surface). Moreover, HPF-FFT operates similarly to other image processing tools used in geomorphological analysis, such as Local Relief Models (Hesse, 2010), Topographic Position Index (Weiss, 2001), relief shadow models (Thelin and Pike, 1991), or other derived models like Openness (Yokoyama et al., 2002), but at a lower computation cost. Nevertheless, two aspects of the method require further analysis before applying it to the extraction of geomorphic references (GRs) of any other morphogenetic relief, which are the main goals of this study.

Firstly, a robust criterion for selecting the cut-off frequencies (COFs[3]) within the frequency spectrum domain should be determined. The COF govern the radius of the circular mask to be applied, and its radius (called filter radius or FR[4] in González-Díez et al., 2021) is seemingly correlated with landform size. Thus, short radius filters detect small-scale geomorphic features, while medium-large radius filters identify large-scale landforms. In relation to the latter, it is worth discussing the scale effects that appear in the FGR. The extensive mapping of high-resolution geomorphic features involves generalisation processes that blur the true limits of isolated features (Gorum et al., 2008; Wheaton et al., 2015). Hence, it is difficult to isolate a single geomorphic feature in relief formed by the combination of geomorphological features of different sizes, as the similarity between FGR and GR is reduced (González-Díez et al., 2021), which affects the uncertainty associated to ground truths (GTs[5]) used in validation tasks, and thereby reduces overall accuracy (Keaton and Haneberg, 2013; Lampert et al., 2016). It is therefore relevant to study how the generalisation process occurs through individual forms.

Secondly, a critical aspect that requires attention is related with the analysis of the high frequency signal. In particular, the effects generated by certain morphologic artefacts, such as those originating from vegetation and anthropic features. Both interfere with the interpretation of small-scale geomorphic features that are present in the relief (González-Díez et al., 2021). The usage of DEMs where the contributions of such artefacts is very limited or null, such as those available for some extra-terrestrial bodies, could provide new insights on how efficient the HPF-FFT is in delineating the true small-scale features (either depressions or hills) present in the terrain model, or how to reduce the noise present in the altimetric signal before applying HPF-FFT methods.

To analyse possible solutions to the above issues, it is important to understand some fundamental considerations of the HPF-FFT methodology and some factors that influence the analysis. As introduced in González-Díez et al. (2021), a DEM can be presented as a mathematical representation ($z(\cdot)$), or a variation of the physical magnitude altitude (z), regarding the independent magnitude space (x,y), being x,y the spatial coordinates of the DEM, where altitudes are the heights of the topographic surface, also called altimetry (Fisher and Tate, 2006; González-Díez et al., 2021; Guth et al., 2021). Hence, when examining the relief depicted in a DEM along any row or column, there can be undulations that usually do not show a cyclical repetition. In other words, the relief has an exceptionally large wavelength (λ), where its fundamental cycle (λ_0) tends towards infinity ($\lambda_0 \rightarrow \infty$). Therefore, it is said that altimetry is an acyclic or aperiodic signal, and FFT[6] offers the possibility of efficiently depicting the altitudes in the frequency domain. In this conceptual frame, the frequency increases as the magnitude of the signal reduces (Gonzalez et al., 2009). By transforming a DEM to the frequency domain through FFT, a strong correspondence could be established between certain geomorphic features and their altitudes (which are expressed by the magnitudes and frequencies of the signal that these geomorphic elements possess). Thus, a systematic search of the FR according to the size of the object registered in the DEM was applied in González-Díez et al. (2021). Subsequently, it was possible to extract the FGRs of the landscape using HPF-FFT filtering based on a Gaussian transference function, which has allowed the mapping of geomorphic units according to scale. This last argument means that although the true magnitudes registered are plotted against the true frequencies, there will be different packages (containing sets of true magnitudes-true frequencies) present in the frequency domain that can be isolated through filtering methods; sets that logically belong to the geomorphic elements that constitute each relief unit. This particularity could therefore constitute an objective basis for identifying these sets, providing a novel approach to the problem and an important strengthening of the method presented in González-Díez et al. (2021).

The Geographical Information System (GIS) and Remote Sensing community understand DEMs as digital representations of elevation values corresponding to a given topographic surface, or the mathematical representation of certain points in either planimetry (x,y) and altimetry (z) on a "bare earth". That is to say, as the surface of any planetary body excluding trees, buildings, and any other artificial surface objects (Garbrecht and Martz, 1999; Guth et al., 2021). However, obtaining such DEMs for terrestrial environments is not a straightforward task. Thus, it is important to recall that quantizing the elevation of a relief is a process where the independent variable takes only integer values $z[x,y]$, the signal is said to be in discrete space and mathematically is said that $x,y \in Z$, where Z is the ring of integers. As with any other physical variable, the quantizing of the signal representing elevations is conditioned by the type of sensor employed (Gonzalez and Woods, 2018) and its design (such as the size of the array or the displacement of the device on the ground surface). For instance, the most recent LiDAR capture sensors record a "point cloud" of millions of individual points on the ground surface with 3D information (Liu, 2008; Kasai et al., 2009). Immediately after the point capture, most of the High Frequency (HF) noise incorporated to the signal is filtered and reduced (this is conducted during the earliest stages of post-processing, and before performing the geometric treatment of the elevation signal). Subsequently, during the mid and final stages of the post-processing, there are attempts to erase artificial elements by filtering (Kasai et al., 2009; Werbrouck et al., 2011). However, many of the artificial elements and the vegetation present on the surface (hereafter called outer-geomorphic elements, OGEs[7]) persist, introducing artefacts in the DEMs also after post-processing tasks (Fisher and Tate, 2006; Lloyd and Atkinson, 2006; Werbrouck et al., 2011). Therefore, inaccuracies in elevation values could remain in the final DEM (Lohani and Ghosh, 2017). In addition, the signal degrades further, losing 3D information during the conversion of the point cloud into a raster file (Garbrecht and Martz, 1999; Guth et al., 2021). In conclusion, despite the described clipping of the HF signal, occasional OGEs may persist in the signal and influence its interpretation. Some of the aforementioned defects could be avoided using Planetary DEMs (PDEMs[8]) from other planetary bodies than the Earth (Guth et al., 2021), because OGEs directly do not exist or are minimal, offering an alternative scenario to check the graphical response provided by HPF-FFT filters.

In view of these considerations, the Moon offers great possibilities to evaluate this methodological approach. Its landscape offers a great diversity of relief units, showing different morphologies, sizes, and relief polarity, either in flat areas, slopes, or summits, where depressions generated by impact craters are the main geomorphic feature (Robbins,

[2] Filtered Geomorphic Reference
[3] Cut-off Frequency
[4] Filter Radius
[5] Ground Truth
[6] 6 Fast Fourier Transform
[7] Outer-Geomorphic Element
[8] Planetary DEM

Table 1
Summary of the methodological framework conducted in this study. Section A. Aims of the three experiments (Experiment_1, Experiment_2 and Experiment_3) conducted indicating the methodological steps carried out. Section B. Objectives and tools of the methodological steps (steps) carried out. Section C. Main indicators of the accuracy assessment conducted. Details of the elements and indicators of the accuracy assessment are presented in Table A.1. Section 1; whereas the rest of details of the methodological framework carried out in each experiment are presented in Sections 2, 3, 4 (Appendix A).

Section A

Experiments performed (Exp_#)	Aims	Steps
Exp_1	Validate the goodness of this type of filtering to identify the morphological boundaries of a flat-bottomed crater.	1…7
Exp_2	Validate the morphological response of an HPF in an emulated cratered landscape, formed by a mixture of craters of different sizes, which may or may not overlap each other's was studied in this section. This experiment has two parts:	
	First: The individual response of each filter to detect craters of a given size was analysed;	1…7
	Second: The effects realised by a combination of sizes were analysed.	1…7
Exp_3	Validate the morphological response of an HPF in a real relief, to test the effective utility of the proposed methodology maintaining the structure of the two previous experiments.	1…8

Section B

Methodological steps	Objective	Tools
1	Creating a SDRM model of a flat-bottomed crater	Script_1
2	Creating a GT employing the SDRM	Arctools
3	Identifying the relevant frequencies contained in the SDRM_1	Script_4
4	Obtaining Filtered DEMs	Script_5
5	Exporting filtered DEMs to the GIS	Arctools
6	Performing a spatial analysis between GT models and Filtered DEMs	Arctools
7	Performing an accuracy test for each scenario	Arctools
8	Performing geomorphic units	Arctools

Section C

Expression	Term	Description
$GA = \frac{\sum A_{i,j}}{N}$	Global Accuracy (GA)	It is the probability of being correctly classified. This index overestimates the accuracy of the classification, as it does not consider either errors of omission or commission.
$Kappa = \frac{N\sum A_{i,j} - \sum nx_{i+} * nx_{+j}}{N^2 - \sum nx_{i+} * nx_{+j}}$	*Kappa*	Kappa statistics, are used to control those instances that may have been correctly classified by chance and were employed in order to assess the spatial correlations between the respective considered limits:

2019). There are limited active surface dynamics capable of modifying the traces left by impact forms. Besides, Moon has an extensive cartographic database, which includes: highly accurate PDEMs (Neumann et al., 2011; Smith et al., 2011; Baker et al., 2016); images and remote sensing data from the Japanese SELENE (Kaguya) mission (Kato et al., 2006; Haruyama et al., 2008; Matsunaga et al., 2008; Ohtake et al., 2008); a complete geological database at 1:5,000,000 scale (Fortezzo et al., 2020); and diverse crater inventories (Head et al., 2010; Salamuniccar et al., 2014; Neumann et al., 2015; Wang et al., 2015; Povilaitis et al., 2018; Robbins, 2019). This database, readily accessible to researchers (Astropedia, 2021a), allows the construction of GTs for further validating purposes. However, crater inventories present limited possibilities to serve as a cartographical basis for the construction of GTs for validating the graphical response extracted from the filter because they present only the centroids of the inventoried craters or their enveloping circles.

Although lunar PDEMs solve part of the problem relative to OGEs, the combination of landforms with assorted sizes could generate blurring and generalisation issues when filtering small-scale elements. Thus, the correspondence between FGRs and geomorphic features of different sizes must first be validated. Synthetic Digital Relief Models (SDRMs[9]) could provide not only a means to explore whether the landscape is composed of relatively simple landforms, such as a depression generated by a single crater, or by a combination of landforms generated by individual elements of known shape and different sizes, but also to objectively analyse this correspondence. Synthetic models have been used before in geosciences (Di Fiore, 2010; Darishchev and Guérillot, 2017; He et al., 2021). In this work, a SDRM is understood as an artificial DEM, which presents simplified morphologies of the reality, such as simple impact craters present in the lunar landscape.

This paper reframes and improves the hypothesis presented in the González-Díez et al. (2021) by introducing a new filtering method based on the extraction of dominant frequencies in the frequency spectrum of the altimetric signal; a true magnitude–true frequency plot is used to select these frequencies from the harmonics that compose the altimetric signal and identify their limits, which will be used as COFs or FRs. Then, HPF-FFT filtering is applied using a Butterworth transfer function that has a wider spectrum than those employed in González-Díez et al. (2021). SDRMs, obtained by the combination of simple craters emulating the lunar landscape, are used to analyse the correspondence between FGRs and landforms and blurring effects. Both the filtering and the design of SDRMs can be developed in MATLAB. After addressing the ability to identify FGRs in simulated synthetic models, real reliefs of densely cratered areas of the Moon will be evaluated. Finally, the correspondence between FGRs and GTs extracted from PDEMS from the existing cartographies, databases, and ad hoc inventories will be validated following González-Díez et al. (2021), to understand the correspondence between these objective references and the main forms sculpted in the relief.

The purpose of this study is not to discuss the advantage of our proposal over others existing in the literature about methods for obtaining inventories of cratered areas, but to validate the usefulness of HPF-FFT to identify the FGRs corresponding to different relief domains, whereof all the possible landforms that could appear on a planetary body, the crater-shaped depressions are the most common geomorphic feature in accordance with different authors (i.e. Melosh, 1989; Hiesinger and Head, 2006; Robbins, 2019). Undoubtedly, the availability of

[9] Synthetic Digital Relief Model

Table 2
A Summary of geometrical characteristics of the Moon DEM. (Lunar_LRO_LOLA_Global_LDEM_118m_Mar2014). Additional details of Moon DEM are presented in Table A.2.

Source	LRO
Type of altimetry data	LiDAR
Resolution	256 pixels per degree
Scale at equator	118.45 m /pixel
Horizontal accuracy	20 m
LiDAR vertical accuracy	0.1 m
Heights converted to lunar	1737.4 m
radius	1 m
LOLA DEM Heights accuracy	6.5 billion measurements gathered between July 2009 and July 2013, adjusted for consistency in the coordinate system described below, and then
Source data	converted to lunar radii (Mazarico et al., 2012).

objective procedures for the mapping of relief elements is another key interest in planetary geomorphic mapping developed through robotic sensors.

2. Methodology

The methodology applied in this research (Table 1) includes improvements over that presented in González-Díez et al. (2021) that are described in the following sections. The signal captured in a DEM was filtered using HPF-FFT methods. By using this filtering, the FGRs of the existing craters' shape relief units are highlighted, facilitating their mapping. The result was then compared with a GT to evaluate the success. This GT was obtained from images and/or geomorphological maps previously acquired from literature or ad hoc research. An accuracy test evaluates the goodness of the fit between FGRs and GTs. In case the reader requires additional explanations on FFT methods and/or conceptual explanations related to DEMs filtered using HPF by the Fourier transform, the authors recommend following the methodological explanations presented in Gonzalez et al. (2009) and González-Díez et al. (2021).

The criterion followed to obtain GTs was purely morphological: all map units included in the depression were part of the crater depression, while those located outside were non-crater; a vector delimits both types of units. The GT classification was performed using the ArcScene 10.8.1 (ArcGIS, ESRI). The pixels belonging to the crater (valued as value_1) were differentiated from those classified as non-crater (value_2).

Once the frequencies in the altimetric signal were identified and the filtered DEMs extracted, they were incorporated into ArcMap 10.8.1 (ArcGIS, ESRI). The respective zero contour lines extracted from each filter plus the DEM edge line were combined and transformed into polygons. These were divided into two classes using the same type of morphological criterion: polygons considered as craters (value_100) and non-craters (value_200). The next step was converting the polygons to a raster, increasing the resolution of the pixel size to 0.1 to reduce the uncertainty in the detections of limits. Accordingly, the same resolution was applied to GT models. Each combination of GT and filtered DEM was called scenario.

The accuracy assessment applied is detailed in Table A.1 Section 1 (Appendix A). To show the adequacy of the results for each scenario, different accuracy indicators were calculated, including Global Accuracy (GA[10]) and Kappa value (Table 1). Finally, two graphs indicating the variations of these values were presented to support the evaluation of the results.

This methodological framework incorporates specific improvements to the overall methodology, which are presented in the following subsections. The first is oriented to introduce the programming tools employed, mainly open-code software combined with ArcGIS (10.8.1) and Microsoft Excel 2016. The second is tailored to understand the graphical response provided by the filtering in cratered areas. The third and fourth subsections are aimed at improving the filtering criteria. The third explains the incorporation of a more robust selection criterion of the frequencies to be filtered, while the fourth proposes how to work with the Butterworth transfer function and extract the graphical responses provided by the filtering. The fifth describes the steps conducted in each of the three experiments for the validation of the graphical response provided by the filtering, including explanations of the criteria used to obtain the GTs. Finally, the sixth subsection shows a description of the lunar territory used in the third experiment.

2.1. Open-code scripts

The application of the basic methodological framework can be performed directly, employing remote sensing programmes, such as ERDAS IMAGE 2020 combined with ArcGIS. In this contribution, a different pedagogical approach, using programming packages designed in MATLAB R2021b and/or Microsoft Excel 2016, was achieved. The aim is to present FFT filters in a more didactic approach, developing scripts such as those generated in MATLAB R2021b for signal analysis (Gonzalez et al., 2009; Gonzalez and Woods, 2018). Most of the code is presented in this paper (see Appendix B), except two scripts that are freely available on GitHub (González-Díez et al., 2022a, 2022b).

2.2. Synthetic models employed

Using PDEMs allows the elimination of the high frequency effect caused by OGEs, which logically affects the interpretation of the filtered signal. The Moon DEM derived from the Lunar Orbiter Laser Altimeter (LOLA) offers a 3D signal generated by billions of accuracy measurements (Table 2) with high geometric-geodetic robustness (Neumann et al., 2011; Mazarico et al., 2012; Astropedia, 2021b). The relief represented by this type of real models is too complex, as it contains dozens of craters of different shapes and sizes. Using such matrices in most existing scripts is not complicated. However, many of the scripts developed for 2D FFT analysis recommend the use of square signal matrices of even order (equal number of rows and columns) and with base 2. Therefore, the isolation of one crater, by trimming the matrix and satisfying the aforementioned conditions, introduces difficulties in the selection and the cut handling of the area to be removed. Therefore, to understand the correlations between a geomorphic feature that generates depressions and the graphical response from FFT filtering, the use of simplified DEMs that emulate the shape of a crater is required. Three types of SDRM of cratered landscapes were used in this work.

The first was used as a basis for studying the morphological response of a relief comprising a single flat-bottomed isolated crater (Chappelow and Sharpton, 2002). The relief was generated using a circular cosine-wave propagation function, in which the period and frequency can be controlled. The details of the parameters employed in the model are explained in the description of Experiment_1 (Table A.1, Section 2, of Appendix A), while the script used to generate the synthetic relief (script_1) is presented in González-Díez et al. (2022a). The code exports an ASCII DEM, with and without a geo-referenced header, which allows

[10] Global Accuracy

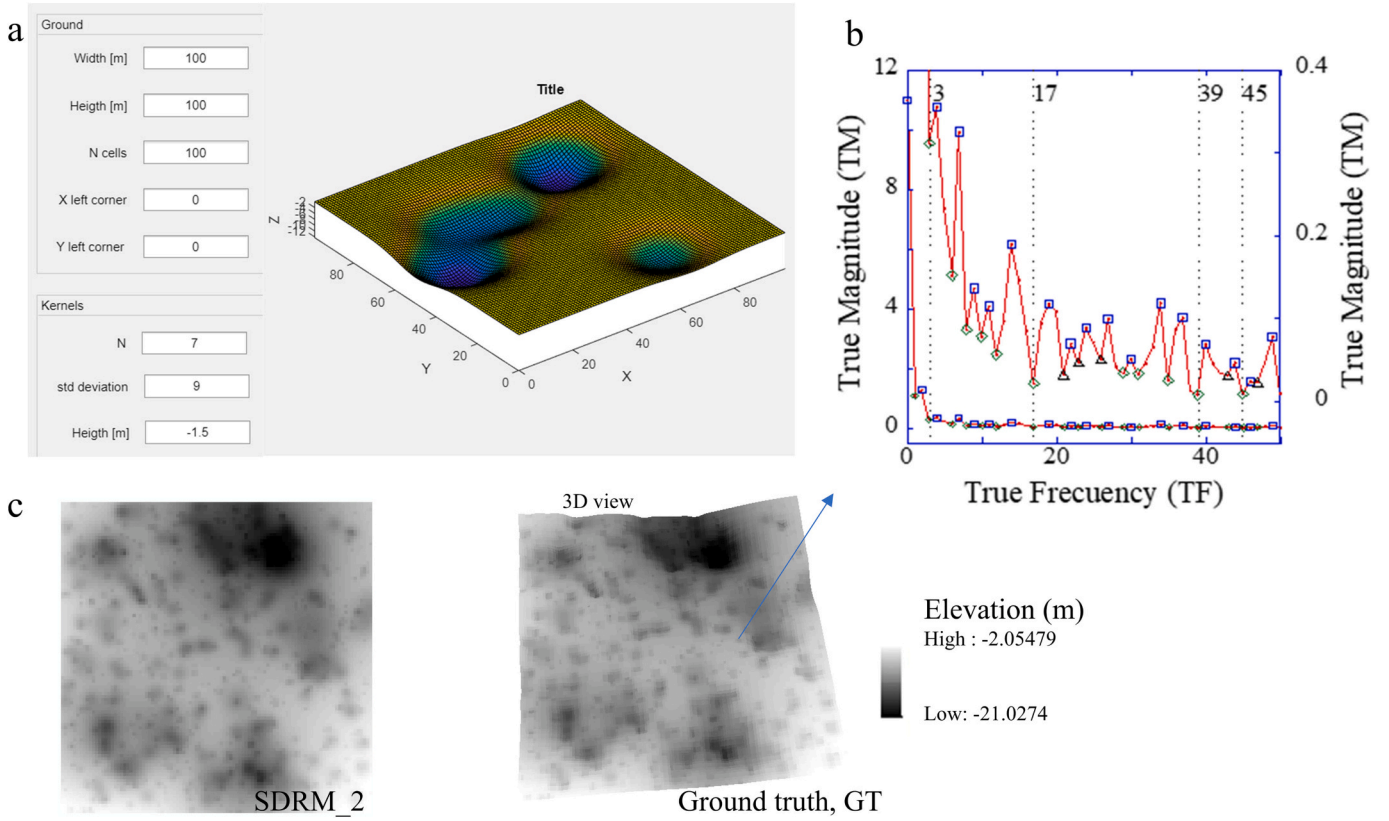

Fig. 1. Four details of Experiment_2: (a) visualization of the GUI developed to create SDRMs from a cratered area; (b) TM-TF plot extracted for the addition SDRM presented in next section; (c) 2D and 3D views of the SDRM_2, employed as Ground Truth (GT). Input boxes of the GUI are: width and height (mesh size in model units); N cells (number of pixels in row or column); X left corner and Y left corner (X and Y coordinates of the bottom left corner of the model); Kernel number (number of kernels used); std. deviation (standard deviation of kernel values); height (height of the kernel). The location of turning points identified in the TM-TF plot are: maximum (squares); minimum (diamonds). The minima magnitude points that are used as COFs are highlighted in the TM-TF plot (vertical dotted lines). These are later used as filter radius, FR. The small harmonic components of the signal (triangles) can be seen as well. They are identified when, in a group of minima, the following has more magnitude than preceding, towards higher frequencies.

subsequent filtering treatments to be undertaken.

The second synthetic model was developed to emulate a cratered landscape (as found in lunar scenes) and was used for studying the morphological response of the filtering on a relief composed by a mixture of bowl shape craters of different sizes, which may or may not overlap. This synthetic model was generated through a MATLAB Graphical User Interface, GUI (González-Díez et al., 2022b), that considers the number of craters to be simulated (script 2), their size (regulated through the standard distribution, st), and their depth (Fig. 1a). The GUI generates a raster DEM, where each elevation point (z_j) includes planimetric coordinates (x_j,y_j). In this GUI, kernels (i), bell-shaped curves, appear (Gaussian kernels) where the elevation of each point can be calculated by applying Eq. (1).

$$z_j = H \cdot \sum_{i=1}^{n} e^{-\frac{1}{2}\frac{\left(x_j-\mu_{xi}\right)^2+\left(y_j-\mu_{yi}\right)^2}{\sigma^2}} \quad (1)$$

The centre of each kernel randomly appears $\left(\mu_{xi}\mu_{yi}\right)$ within the DEM limits. Then, for each DEM point with coordinates $\left(x_j, y_j\right)$, its elevation z_j is obtained. To evaluate the method, the user defines the height and size of the grid (which corresponds with distance between two adjacent planimetrical coordinates); the height and width are in the corresponding units (e.g., millimetres, metres, or kilometres). The DEM resolution is defined by the number of cells dividing the ground, and the coordinates were calculated from the bottom left corner. Finally, the kernels were summed. The user selects the number of kernels, n, to add and their shape, defined by the standard deviation, σ, and height,H. Note that if H is positive, the kernels are added as hills, but if H is negative, they are subtracted and are depressions. As well as in the later code, the GUI exports an ASCII DEM, with and without a geo-referenced header for further treatment. Some details of how this model was employed are explained below in the description of experiment 2 (Table A.1, Section 3, of Appendix A).

The third synthetic model (called Testing matrix) was developed to evaluate the suitability of the filtering described in the next Subsection 2.3. The model was constructed using a linear harmonic function of sinusoidal type (script_3, of Appendix B) for validating the next script (script_4, of Appendix B), which will be described in the following section. In this way, the model maintains the harmonic series in rows and columns, preserving the magnitudes and frequencies.

2.3. Extracting cut-off frequencies (COFs) from the true magnitude-true frequency plot

The true magnitude-true frequency plot (hereinafter referred to as TM-TF plot[11]) arises from the need to find a more robust selection criterion for filtering frequencies than that used in González-Díez et al. (2021). By plotting the true magnitude (also called amplitude in scripts) against the true frequency, it is possible to acquire an overview of the different frequency components that comprise the whole DEM-signal, showing the principal existing harmonics in the relief. The graph represents a sawtooth-shaped function (Fig. 1b), with a set of maxima and

[11] True Magnitude-True Frequency plot

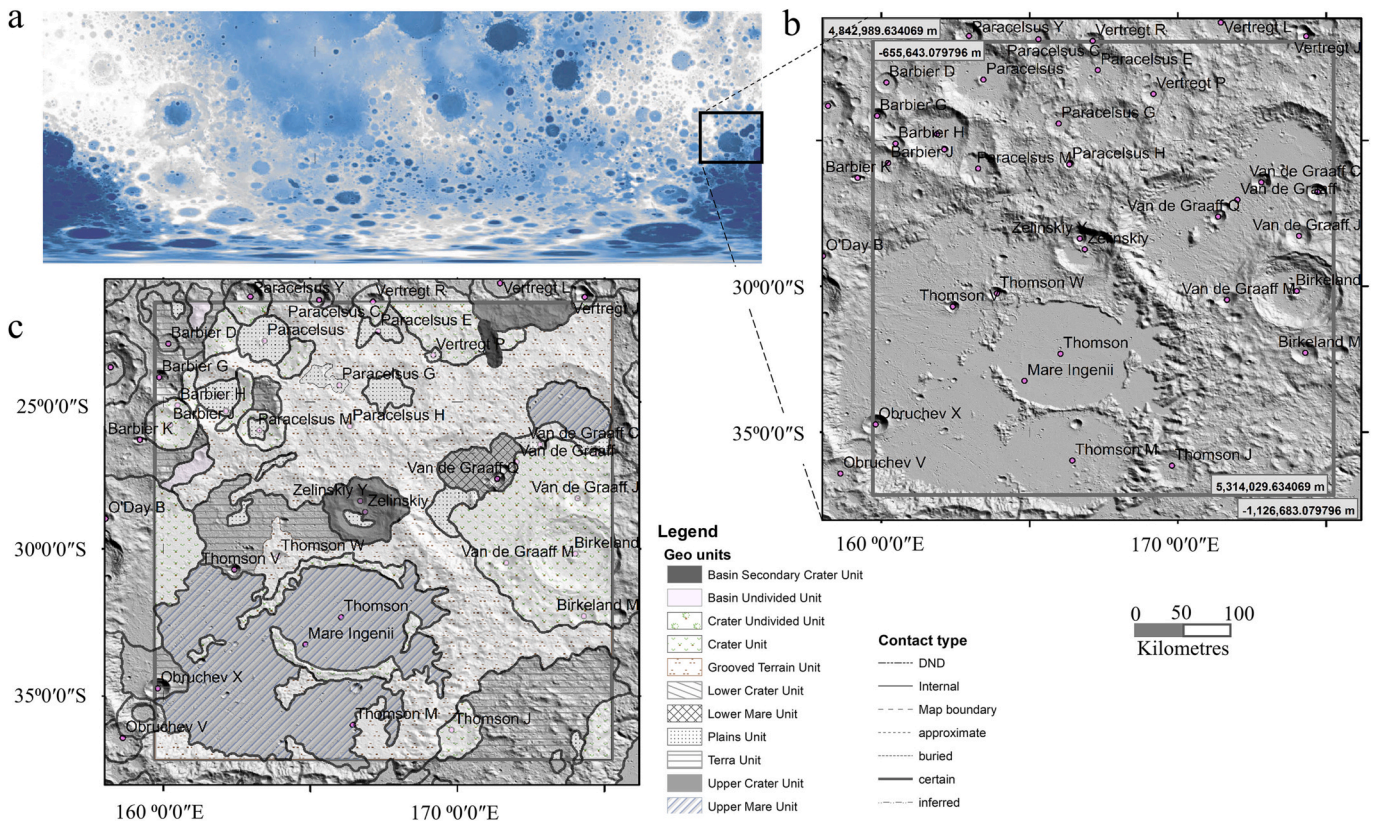

Fig. 2. Main characteristics of Mare Ingenii (used in Experiment_3), showing: (a) location of the study area (black box line) on the lunar surface cartography of ArcGIS (ArcMap 10.8.1) Map Service (https://tiles.arcgis.com/tiles/cuQhNeNcUrgLmYGD/arcgis/rest/s); (b) DEM extracted from the LOLA tile; (c) geological units defined in the area. The projection system employed in section a is present in Table A.2 (GIS coordinate systems A). The LOLA of the Mare Ingenii area is named as *1 (the model has been projected in a flat representation system presented in Table A.2 (GIS coordinate systems B), using a background constructed by a shade relief named *2. The geological units of section c come from Fortezzo et al. (2020).
*1, Lunar_LRO_LOLA_Global_LDEM_118m_Mar2014_clip_zonal_clippings4096_e4_int.tif;
*2, Lunar_LRO_LOLA_Global_LDEM_118m_Mar2014_clip_recortes_zonales4096_e4_hillshade45_45.img.

minima that progressively decrease in magnitude as the spatial frequencies increase. In such a representation, each maximum magnitude corresponds to the dominant frequency, while the adjacent minima (preceding and following the maximum) constitute the smallest frequency values around it. By analysing the whole signal, in terms of magnitude, different frequencies are detected. Two adjacent minima delimit a set of harmonics existing in the signal, where the maximum gives the representative value of each set. Each pair of minima represents a change in the trend of the frequencies. In addition, there may be small subsets within a group (Fig. 1b). Therefore, the relevant harmonic sets could be identified by the greatest variations in magnitude/frequency; and their minimum can be used as a reference to identify COF. These sets of frequencies could correspond with the main FGRs and their use as FR should be highlighted. A script for obtaining the TM-TF plot from a DEM in raster format was created (script_4, of Appendix B) and incorporated to the Appendix.

2.4. Applying Butterworth transference function

As demonstrated in González-Díez et al. (2021), a HPF using FFT with a Gaussian transference function enables the analysis of those parts of the altimetric signal where changes in altimetry appear abruptly, as found in a cratered relief. The need to find a more correct emulation of the reality requires the analysis of other transference functions. In this study, a Butterworth type transference function, *H(u,v)*, was utilised. The Butterworth function employed (Eq. (2)) considers an order n equal to 1, where *H(u,v)* reduces at 50 % of the maximum at D_0.

$$H(u,v) = \frac{1}{1 + \left[D(u,v)/D_0\right]^{2n}} \quad (2)$$

The advantage of using Butterworth functions is twofold. The Butterworth filter exhibits a Gaussian type transference function that transforms into an Ideal shape as n increases, with no ringing effects around the edges (Gonzalez et al., 2009). Moreover, in literature there are many MATLAB scripts written for performing FFT filtering, in which it is possible to analyse either 1D or 2D signals, applying LPF or HPF, selecting different transference functions as Ideal, Gaussian or Butterworth (Irg1994, 2012; Geeksforgeeks, 2021; Regina, 2021). In our study, the set of codes presented in Regina (2021) developed to filter a 2D signal (called script_5) have been applied.

2.5. Description of the experiments performed

Three experiments (Experiment_1, Experiment_2, and Experiment_3) evaluated the capability of the above HPF-FFT for detecting relief domains with crater-shaped depressions. All three experiments have the same methodological framework, but in each, some modifications were incorporated to achieve the previously presented aim (Table 1). The specific methodology according to the objectives pursued in each experiment is presented in Tables A.1, Sections 2, 3 and 4 respectively (Appendix A), additionally presenting the similarities between them.

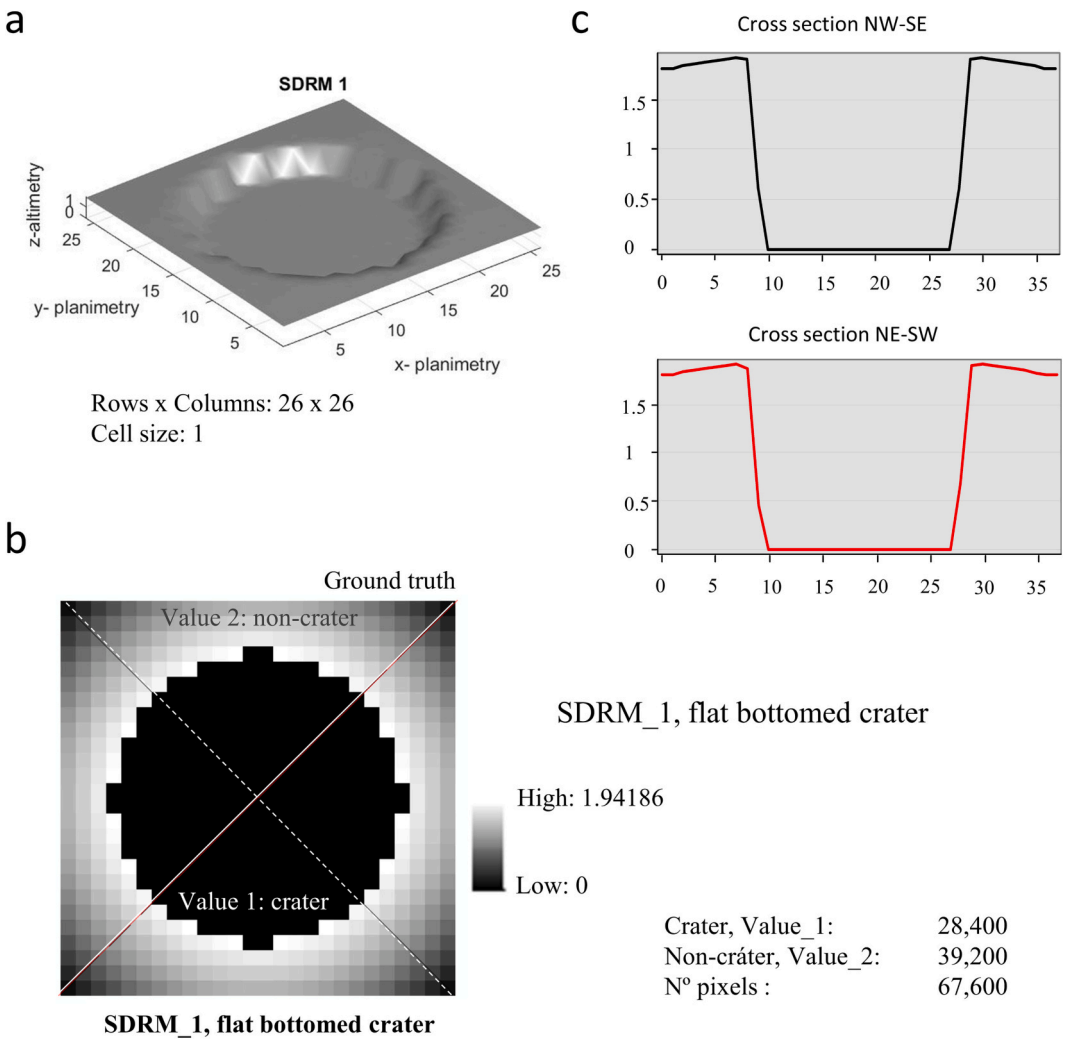

Fig. 3. Three details of SDRM employed in Experiment_1, showing: (a) SDRM_1 belonging to a flat-bottomed crater, indicating the number of rows and columns that compose such model; (b) plan view of the SDRM_1 showing the location of two diagonal cross-sections employed to describe its morphology, which are presented in the next section; (c) two diagonal cross-sections illustrating the crater morphology. The Ground Truths (GT) elaborated using the SDRM_1 are classified as craters (value_1) and non-craters (value_2).

2.6. Lunar study area employed in Experiment_3

The selected lunar study area is named Mare Ingenii and corresponds to a 235,393 km^2 basin, centred at about 30°S and 167°E (Fig. 2a-b). This area corresponds to a square-clipped grid of 4096 × 4096 of the Lunar_LRO_LOLA_Global_LDEM_118m_Mar2014 (called Mare Ingenii DEM), which provides an accurate global coverage (Neumann et al., 2011). A detailed description of this dataset is available at Astropedia (2021b). The resulting topographic map of LOLA DEM has become the geodetic frame of reference for the lunar research community and is the highest resolution and most accurate DEM to date (Baker et al., 2016). Additional DEM characteristics and how they have been introduced in the GIS are presented in Table A.2 (Appendix A). In summary, the aforementioned DEM is built from data captured by NASA's Lunar Reconnaissance Orbiter, LRO (Chin et al., 2007; Robinson et al., 2010; Tooley et al., 2010), which is equipped with two cameras that serve as a scanner, generating line-by-line images of the lunar surface, and a laser altimeter called LOLA, besides other sensors also incorporated on the platform. The DEM has a resolution of 256 pixels per degree; at the equator, the pixels have an approximate size of 118 m (in projection). It is constructed with elevation data captured by the altimeter (between July 2009 and July 2013), adjusted to the Lunar coordinate system and converted to lunar radius (Mazarico et al., 2012). The DEM offers a 2D signal of highly accurate geodetic elevations (Grumpe et al., 2014); the average accuracy of each point is >20 m in horizontal position and ~1 m in radius. However, it also contains some imprecisions (Baker et al., 2016); gaps between tracks of 1–2 km are common, sometimes reaching up to 4 km near the equator. To address this shortcoming, interpolation procedures were applied to fill the DEM points in these gaps (Smith et al., 2011). From a data storage perspective, this is a large model with over 7 Gb of information (Neumann et al., 2011). The selected area (Fig. 2b) is perfectly square (row length: 485,173.60 km). A hillshade relief model was created using this clipped DEM by placing the sunlight at an azimuth of 45° with a 45° tilt. This shaded relief (Fig. 2b) appears as background in all graphical outcomes presented for this experiment.

Geological information is taken from the Unified Geologic Map of the Moon, at scale 1:5,000,000 (Fortezzo et al., 2020), which was created in a GIS environment and available at Astropedia (2021c). Using the GIS, the boundaries of the previous maps were compared and the areas of overlap between the poles were integrated. The 203 units identified in the previous maps were integrated into 43 GeoUnits, and divided into the following groups: craters, basins, terra plains, Imbrium Formation, Orientale Formation, and volcanic units. Various surface features were also mapped: crater rim ridges, buried crater rim ridges, fissures, holes, scarps, sea wrinkle ridges, faults (generic, unless the type can be determined), troughs, rills, and lineaments. This cartography is

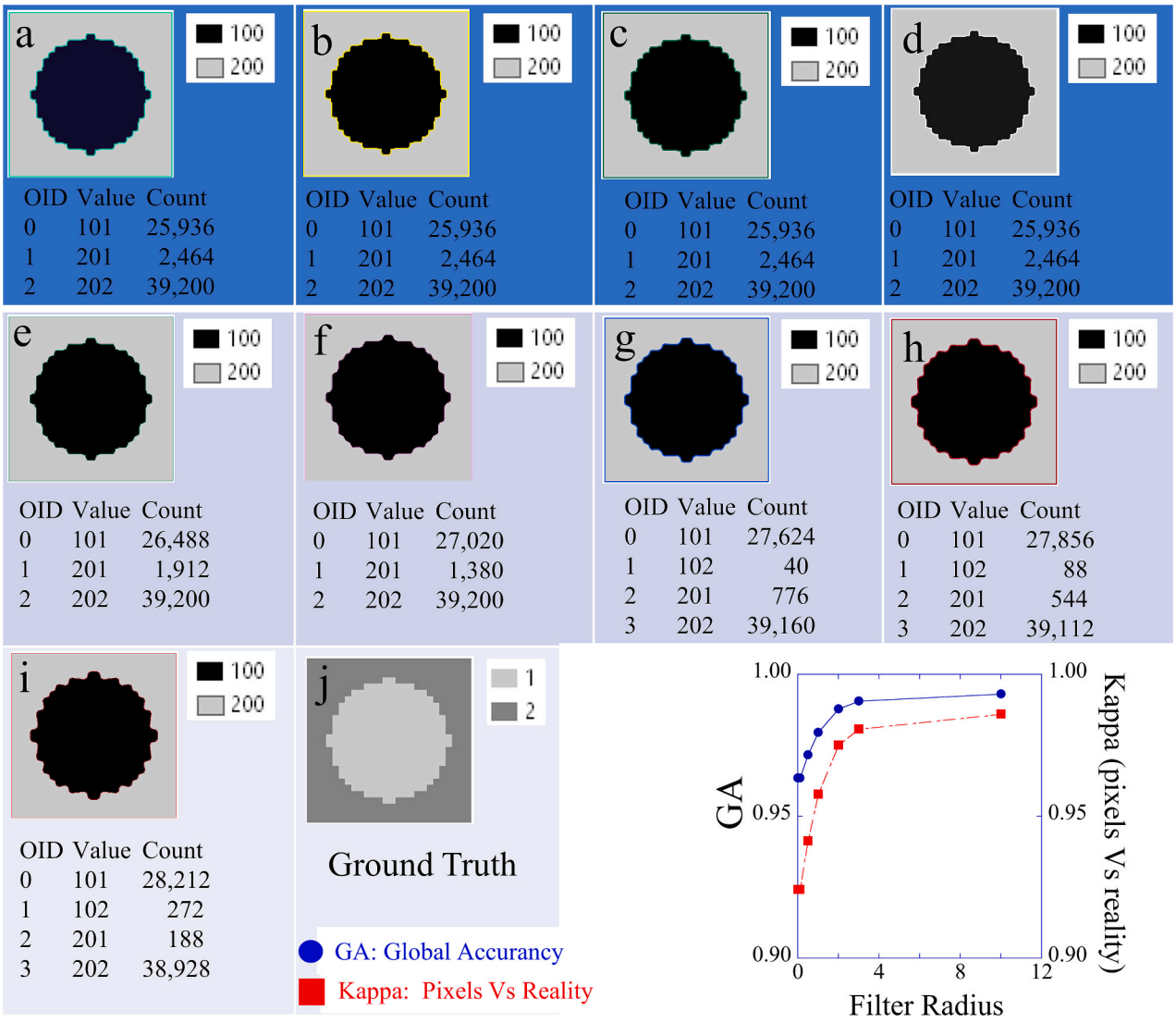

Fig. 5. Results of the combinations performed in Experiment_1 between the filtered models (Fig. 4) and the Ground Truth (GT). Pixels valued as 100 correspond to detected craters, while those as 200 are detected non-craters. Box j includes the GT, where pixels valued as 1 correspond to crater while those as 2 are non-crater. Boxes classified from a to i show the results of the respective crossing map, including the crossing spatial analysis results. Bottom right, results of the accuracy indicators obtained.

supported by existing mapping and data derived from LOLA altimetry (north and south polar, 100 meters per pixel, m/pix) and shaded relief derived from the SELENE Kaguya stereo terrain camera (equatorial, ~60 m/pix). The geological model incorporates solutions to correct positioning and visibility errors. The GeoUnits and feature contacts present in the area used in Experiment_3 are presented in Fig. 2c. An ad hoc crater map was performed using LOLA DEM-derived aspect, shading and slope models to support the crater rim identification. This map solves the limited use of previous crater inventories, as GTs previously mentioned in the introduction. The map produced includes all crater types with a surface area >1 km^2.

3. Results

The results from this study are organised regarding each of the experiments previously presented in Table 1a-c.

3.1. Experiment_1

SDRM_1 (presented in Table 1, and detailed in Table A.1, Section 2) is a square matrix of 676 pixels, showing a flat-bottomed crater shape (Fig. 3a). Altitudes range from zero, in the centre of the matrix, to 1.94 near the crater rim (Fig. 3b). The morphology of its diagonal cross sections shows a profile like an inverted top hat (Fig. 3b-c). Altitudes increase from corners to the edge of the crater depression, and then, suddenly decrease to zero (at the centre of the depression). This pattern

Table 3
A summary of the Global Accuracy and Kappa values obtained from the cross-validation between the Filtered Model (FM) and Ground Truth (GT) in the nine Filter Radius (FR) scenarios analysed in Experiment_1. The full details of the cross-validation data are presented in Table A.3 (Appendix A).

Filter Radius (FR)	Global Accuracy (GA)	Kappa
$1.0e^{-04}$	0.960	0.920
$1.0e^{-03}$	0.960	0.920
$1.0e^{-02}$	0.960	0.920
$1.0e^{-01}$	0.960	0.920
0.5	0.960	0.920
1	0.980	0.960
2	0.988	0.975
3	0.991	0.981
10	0.993	0.986

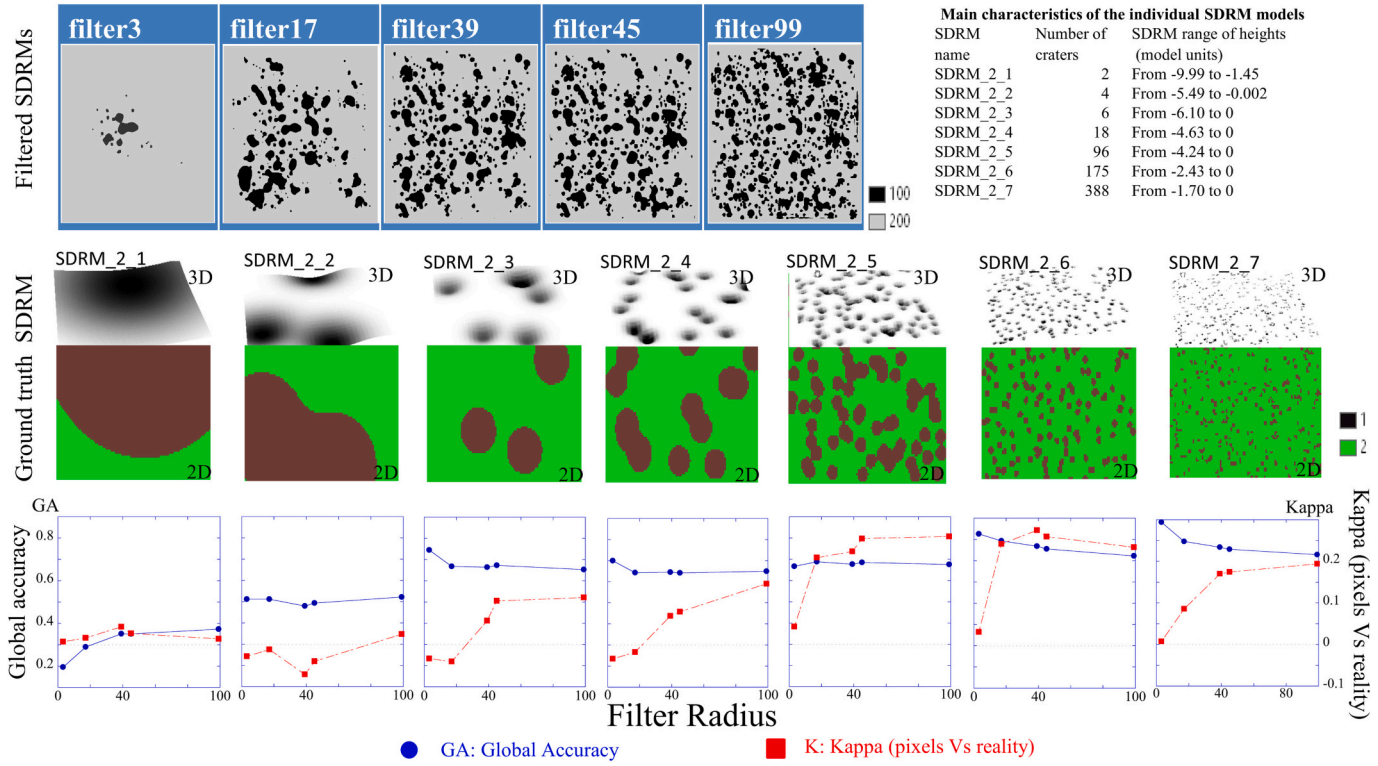

Fig. 6. Results of the combinations performed in Experiment_2 (first part) between the filtered models and the Ground Truth (GT). Upper left filtered SDRMs employed corresponding to the following Filter Radius (FR): 3, 17, 39, 45 and 99. Pixels valued as 100 correspond to detected craters, while those as 200 are detected non-crater. Upper right, the main characteristics of the individual SDRM models obtained by means of the GUI. Middle, 3D (SDRM models) and 2D GT views. Pixels valued as 1 correspond to craters while those as 2 are non-craters. Bottom, results of the accuracy indicators obtained in the respective crossing maps between filtered SDRMs and GTs.

is repeated symmetrically to the opposite corner. The GT model obtained (Fig. 3b) was morphologically evaluated, reclassified and resampled to a pixel size of 0.1. A detailed analysis of the TM-TF plot shows how the true magnitude (TM) decreases from 3.7 to 0 as the true frequency (TF) increases (Fig. 4, Appendix C). The function profile presents inflection points (slope changes) at 1 and 3 TFs, reaching TM values of 0.05 and near zero, respectively. Three set of COFs have been identified at the following TFs: from 0 to 1, from 1 to 3, and above 3. However, to analyse the shape of the TM-TF function, additional filter limits were extracted around these at the following TFs: 10^{-4}, 10^{-3}, 10^{-2}, 10^{-1}, 0.5, 1, 2, 3, 10, 12, and 26. The contours of the FGR obtained with each COF are also presented in Fig. 4. Filters at 10^{-4}, 10^{-3}, 10^{-2} COFs show vectors with a similar spatial distribution between them. All three provide the same cartography at different scales of representation, with no spatial difference. A tenuous spatial shift is visible using vectors provided by the 0.1 filter, with this shift clearly visible using COFs between 0.5 and 10. Above the 10 COF the border is over-passed and FGR vectors generating Gibbs effects are present. The best results are achieved below the 10 COF, providing FGRs of the crater that are clearly identifiable (Fig. 4).

The GT, combined with the polygons extracted from the previous filters, generates nine models. The data of respective combinations between GT and filtered SDRMs are presented in Table 3 and Table A.3 (Appendix A), whereas the accuracy indicators obtained are introduced in Fig. 5. The GA figures show equivalent values for those filters under FR0.1 (FR#[12]), which are close to 96 %. Over that frequency, the GA gradually increases to 0.99 at the 3 TF. In all cases, GA increases accordingly with FR. However, above 3 TF the values show practically 100 % success. Kappa values show a similar behaviour. Thus, from 0 to 0.1 TF, it approaches a value close to 92 %. This means that contacts are real, being essentially unchanged from 3 to 10 TFs.

3.2. *Experiment_2*

Following the methodological guide (Table 1 and Table A.1, Section 3), the first part of the experiment was developed. Seven SDRMs (Fig. 6) were made using the GUI made for this purpose (script_2); an example of the GUI environment used for the construction of SDRM2_3 is presented in Fig. 1a. Using these, another seven GTs were generated as well (Fig. 6). The addition of these SDRMs enables the creation of a new model called SDRM_2 (Fig. 1c), with altitudes in the range of −21.03 to −2.05, which was used in the second part of the experiment. The TM-TF plot of the SDRM_2 is presented in Fig. 1b. The highest TM is over 11 where TF is close to zero. From these values, as the TF increases, TM shows oscillating values tending to 0. Hence, a sudden fall to 0.31 close to the 3 TF; from that point the TM progressively descends to a value under 0.05 at 17 TF. Then, the function maintains an oscillating form. The next minima of magnitude are at 39 TF and the following ones at 45. Therefore, four sets of COFs were identified: 3, 17, 39 and 45. In addition, a new COF was selected at 99 to analyse all the function distributions of the GA and Kappa indices.

The results of the first part belonging to the spatial crossing between individual filtered SDRMs and the GTs (one for each crater size: large, medium, smallest, minimum, etc.) are presented in Tables 4 and A.4 (Appendix A), whereas the GA and Kappa indicators obtained are introduced in Fig. 6. The GA and Kappa values increase as the crater size reduces. The lowest GA values are achieved with the larger crater size (SDRM_2_1), between 0.19 and 0.37, but increasing with the FR. The next crater size model (SDRM_2_2) shows values ranging from 0.51 to 0.52, decreasing a little when using a FR between 39 and 45. Medium size craters (SDRM_2_3) give the highest GA at FR3 (0.746), decreasing

[12] Radius of size#, e.g. FR0.1 is Filter Radius of size 0.1

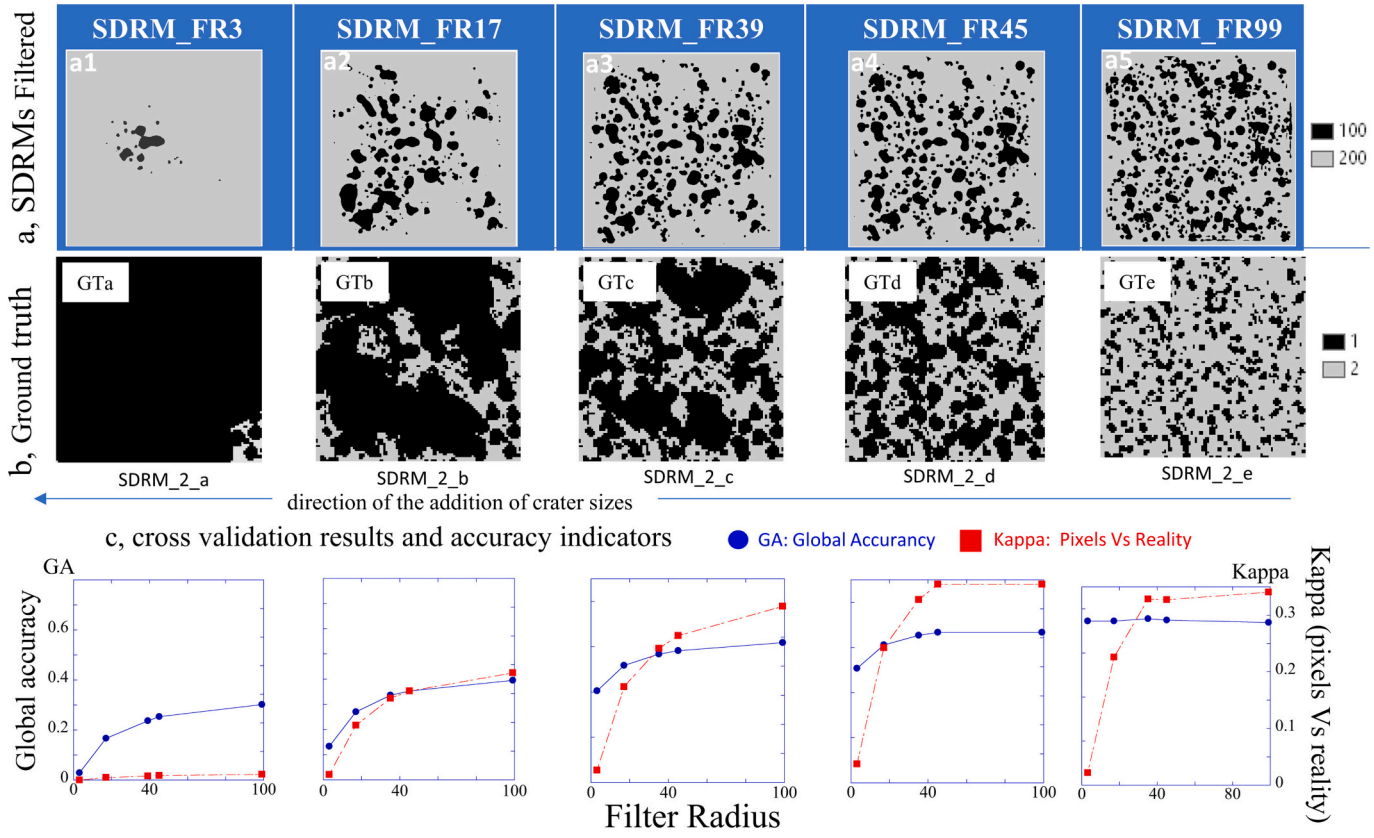

Fig. 7. Results of the combinations performed in Experiment_2 (second part) between the filtered models and the Ground Truth (GT). Upper, filtered SDRMs employed corresponding to the following Filter Radius (FR): 3, 17, 39, 45 and 99. Pixels valued as 100 correspond to detected craters, while those as 200 are detected non-craters. Middle, views of GT employed (*). Pixels valued as 1 correspond to craters while those as 2 are non-craters. Bottom, results of the accuracy indicators obtained in the respective crossing maps between filtered SDRMs and GTs.
*The construction of the GTs is obtained by combining the crater models from the smallest to the largest crater sizes (horizontal arrow). The two smaller ones (SDRM_7 and SDRM_6) were combined into a single model referenced as GTe; similarly, the previous model was combined with SDRM_5 to obtain GTd; then, the previous model was combined with SDRM_4 to obtain GTc; and the previous model was combined with SDRM_3 to obtain GTb; finally, the previous model was combined with SDRM_2 to obtain Gta. SDRM_1 is not employed.

Table 4
A summary of the Global Accuracy (GA) and Kappa (K) values obtained from the cross-validation between the Filtered Model (FM) and Ground Truth (GT) and the Filter Radius (FR) scenarios analysed in the Experiment_2, part1. The full details of the cross-validation data are presented in Table A.4 (Appendix A).

FR	SDRM 2_1		SDRM 2_2		SDRM 2_3		SDRM 2_4		SDRM 2_5		SDRM 2_6		SDRM 2_7	
	GA	K	GA	K	GA	K	GA	K	GA	K	GA	K	GA	K
3	0.20	0.01	0.51	−0.03	0.75	−0.03	0.70	−0.03	0.67	0.04	0.83	0.03	0.89	0.01
17	0.29	0.02	0.51	−0.01	0.67	−0.04	0.64	−0.02	0.69	0.20	0.79	0.24	0.80	0.09
39	0.35	0.04	0.48	−0.07	0.67	0.06	0.65	0.07	0.68	0.22	0.77	0.27	0.77	0.17
45	0.35	0.03	0.49	−0.04	0.67	0.10	0.64	0.08	0.69	0.25	0.76	0.26	0.76	0.17
99	0.37	0.01	0.52	0.02	0.65	0.11	0.65	0.15	0.68	0.25	0.72	0.23	0.73	0.19

Table 5
A summary of the Global Accuracy (GA) and Kappa values obtained from the cross-validation between the Filtered Model (FM) and Ground Truth (GT) and the Filter Radius (FR) scenarios analysed the Experiment_2, part2. The full details of the cross-validation data are presented in Table A.5 (Appendix A).

FR	GTa		GTb		GTc		GTd		GTe	
	GA	Kappa	GA	Kappa	GA	Kappa	GA	Kappa	GA	Kappa
3	0.30	0.01	0.23	0.01	0.41	0.02	0.51	0.03	0.75	0.02
17	0.25	0.01	0.37	0.10	0.52	0.17	0.61	0.23	0.75	0.23
39	0.24	0.01	0.44	0.14	0.57	0.23	0.66	0.32	0.76	0.33
45	0.17	0.00	0.45	0.15	0.58	0.25	0.67	0.34	0.75	0.33
99	0.03	0.00	0.50	0.19	0.62	0.30	0.67	0.34	0.74	0.34

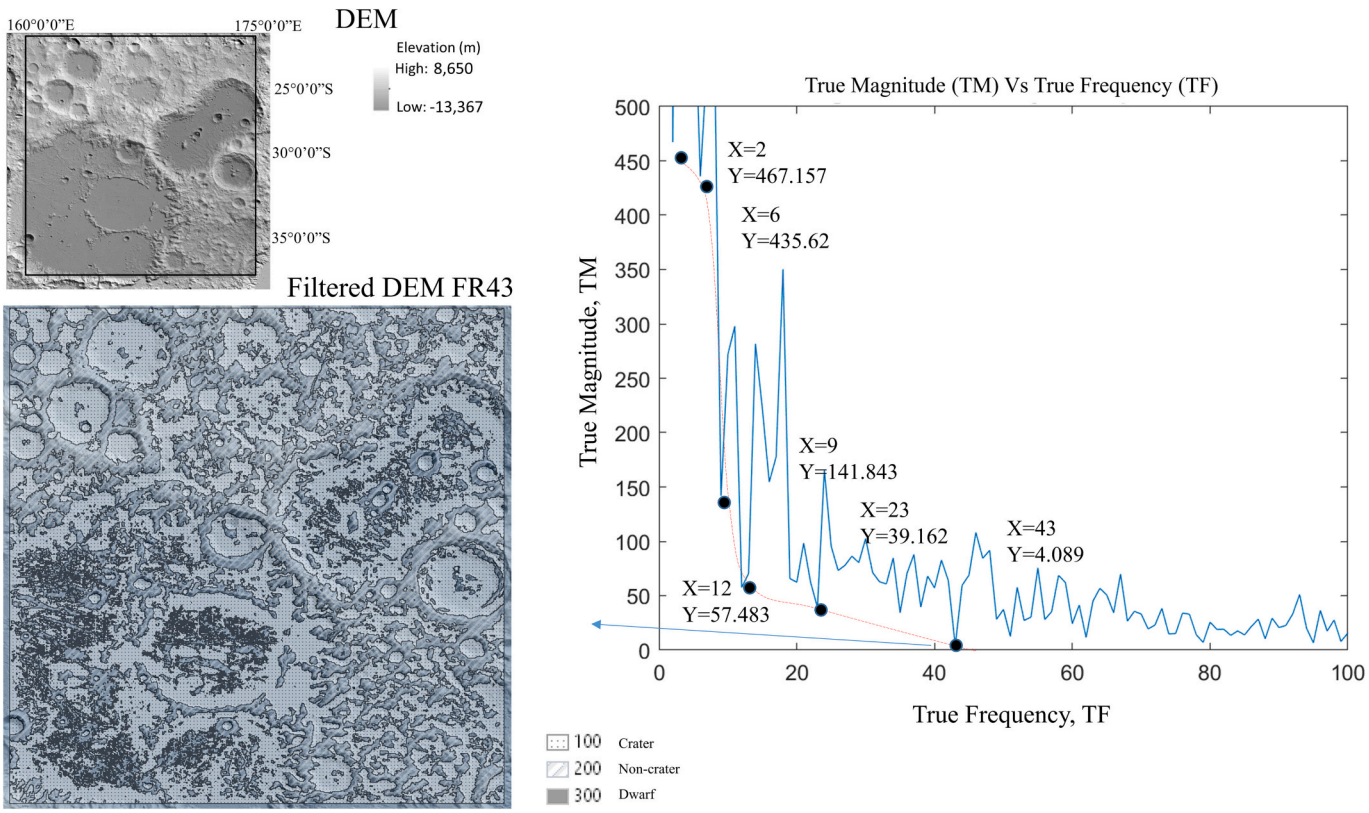

Fig. 8. Three details of the main elements employed in Experiment_3 applying the method proposed. Top left, Mare Ingenii DEM (correspond with a clipping of the Lunar_LRO_LOLA_Global_LDEM_118m_Mar2014_clip_recortes_zonales4096_e4_int.tif, which is a tile of the LOLA DEM), indicating the elevation range (in metres). Right, true magnitude-true frequency plot obtained for the last DEM, indicating: envelope of the values of lower magnitude (dashed line); minimum values identified, indicating their value of X, true frequency and Y, true magnitude (bold dots). Bottom left, an example of the FGR polygons obtained using the Filter Radius (FR) 43 showing the classes obtained (crater, non-crater, dwarf).

lightly as the FR increases, reaching 0.65 at FR99. Small craters (SDRM_2_4) also show values of between 0.70 at FR3 and 0.65 at FR99. Minimum crater sizes models (SDRM_2_5; SDRM_2_6; SDRM_2_7) show similar profile patterns for GA. Values increase as the crater size reduces in all cases, reaching a maximum at FR3 (0.66, 0.82 and 0.88, respectively); and slightly reducing when approaching FR99 (0.67, 0.72 and 0.73, respectively). The Kappa values obtained for each of the cases show a relative increase from FR3 to FR99. The highest Kappa value is 0.25 (SDRM_2_5), while being minor in the remaining cases.

The second part was designed to analyse the response of each filter to detect a relief constructed by a combination of craters of varied sizes, equivalent to a simulated lunar relief. The five GTs (GTa-e) generated in this part are presented in Fig. 7. GTe was obtained through the combination of smallest craters, SDRM_2_7, with the following in size, SDRM_2_6. GTd was obtained grouping the previous GTe with the next crater size, in ascending size order (SDRM_2_5). By repeating this process, GTc, GTb and GTa were generated. The results of the spatial crossing are presented in Table 5 and Table A.5 (Appendix A). The GA values achieved for the five scenarios show an increase while reducing the crater size (Fig. 7) and as FR increases, being slightly similar to the scenario generated by the smallest craters. Regarding Kappa values, these ascend in all scenarios as filter size increases. Moreover, Kappa is progressively higher as the cratered area is composed by sets of smaller crater sets. As in the previous part, the filtering adjusts better as the crater size reduces. Therefore, limits of small craters are more reliable than medium size craters, which are more reliable than large ones.

3.3. Experiment_3. The real case of Mare Ingenii

Following the guidelines of the experiment presented in Table 1 and Table A.1 Section 4, the Mare Ingenii DEM and the TM-TF plot are extracted and presented in Fig. 8. Of all the frequencies shown, those representing the greatest variation in magnitude (1, 2, 6, 9, 12, 23 and 43) were selected as COFs, and used in the script_4 as FRs in the filtering. The ad hoc crater-shaped depression inventory presented in GT4 is composed of 479 elements, with areas ranging from 1 km^2 to 28,736 km^2 (Table 6a). The final trimming was developed to adjust the size of the inventory to the dimensions of the DEM and maintained 464 polygons, of which 463 correspond to craters with sizes within the range described above (Fig. 9a Appendix C).

Using script_5, seven filtered DEMs were extracted with the aforementioned FRs (Table 6b). On this occasion, three classes of polygons were considered: crater, no-crater, and a third called dwarf. The dwarf class contains polygons smaller than 1 km^2. The graphical answers provided by filtering are presented in Fig. 9b-h. The number of dwarf polygons increases exponentially with FR, being close to 50 % of the polygons identified in FR1, and approximately 86 % in FR43. The dwarfs corresponding to filters from FR1 to FR6 are principally in uplands and intra-crater ridges (Fig. 9b, d); while those corresponding to the rest of the filters (FR9 to FR43) are mostly in the Maria region (Fig. 9e-g). An interesting aspect of the study of the spatial distribution of the filtering vectors in the three experiments performed is that the FGRs show similar behaviour in the crater-shaped depressions and uplands (Fig. 10).

The eight GTs considered (Fig. 11), of which the selection is presented in Table A.1 Section 4 (Step_2), include either those derived from the lunar geology (Fig. 11a-c), those extracted from the ad hoc inventory

Table 6
Main results of the following crater inventories performed: a, ad-hoc crater inventory performed by the research teams using traditional cartographic methods; b, inventory of the FGR assigned to crater, non-crater and dwarf using the filtering method described; c, hits obtained in the correlation between centroids of ad-hoc inventory and the FGRs centroids using the Euclidean distance of FGR centroids.

a, ad-hoc crater inventory performed

Nº of craters	Characteristics, crater sizes	Mean radius/m
68	Depressions smaller than 2 km^2	> 736
38	Larger than 2 and smaller than 3 km^2	~995
160	Larger than 3 and smaller than 10 km^2	1,445
160	Larger than 10 and smaller than 100 km^2	2,965
41	Larger than 100 km^2 and smaller than 1000 km^2	9,500
12	Larger than 1000 km^2	62,983
479 total		

b, inventory of the FGR assigned to following geomorphic features

Filter Radius, FR	Polygons	Crater					Non crater	Dwarf
		Number of craters detected from ad-hoc inventory						
		Size/km^2						
	Total	Total	*<2*	*>2≤10*	*>10≤100*	*>100*	Total	Total
FR1	210	37	*9*	*7*	*10*	*11*	59	114
FR2	252	35	*3*	*5*	*11*	*16*	98	119
FR6	559	52	*0*	*5*	*24*	*23*	128	379
FR9	1,246	70	*4*	*17*	*21*	*28*	247	929
FR12	1,985	107	*4*	*34*	*36*	*33*	260	1,618
FR23	5,966	167	*30*	*69*	*38*	*30*	743	5,056
FR43	11,542	315	*91*	*131*	*55*	*38*	1,247	9,980

c, hits obtained in the correlation between centroids of ad-hoc inventory and the FGRs using the Euclidean distance of FGR centroids as distance reference

FGR	Crater size / km^2						
	>1000	*>100 < 1000*	*>10 < 100*	*>2 < 10*	*>1 < 2*	*<1*	Totals
FR1	5	14	53	49	8	4	133
FR2	1	17	33	27	4	3	85
FR6	2	16	37	35	4	1	95
FR9	5	16	36	28	6	1	92
FR12	6	20	43	25	9	1	104
FR23	4	21	51	49	10	1	137
FR43	5	21	71	75	14	1	187

(Fig. 11d), those generated in a combined way (Fig. 11e), or those with a deliberate error in the non-cratered units (Fig. 11f-h). Regarding the ad hoc inventory, its transformation into a polygon map, including crater and non-crater classes, has generated a new inventory with 451 units.

The results of the spatial crossing between filtered DEMs and the individual GTs are presented in Table 7, whereas the GA and Kappa indicators obtained are introduced in Fig. 11. Those GTs corresponding to large craters give both elevated GA and Kappa values (Fig. 11a-b). The analysis performed shows the effectiveness of filters in detecting shapes corresponding to large craters, non-craters and dwarves. Concerning craters, using the centroids of the ad hoc inventory and the FGRs that were extracted from filtered DEMs, the hits between both types of centroids were registered in Table 6c. The correlation uses the Euclidean distances of the FGRs; therefore, the criteria employed were that an ad hoc centroid located in the inner rings of the proximity model was considered as a hit. The results, ordered according to the crater size, show an increase in success with the FR, and increase as the crater size reduces, in exception to those belonging to the range between FR2 to FR12, which have less sensitivity to the craters' identification regarding the previous results. Therefore, as the FR increases, the number of craters detected increases as well, although the crater radius decreases.

The definition of a model of relief domains is also possible. The results show an automatically constructed moonscape that contains three relief units (Fig. 12), exhibiting an enormous coincidence with the relief depicted in the lunar geodatabases, demonstrating its potential usefulness for moonscape characterisation.

4. Discussion

In this section, a discussion of the results previously presented is given, following the same structure, one part for each experiment.

4.1. Discussion, Experiment_1

The function incorporated to script_1 provides great versatility to simulate these types of morphologies. Thus, in this experiment, using a sample frequency = 0, a small, flat-bottomed depression has been generated for the testing; although in future experiments, depressions with a peak in the centre (sample frequency = 2), or others composed of "n" wavefronts (sample frequency = n) can be modelled. The analysis of the frequencies that compose the signal, using script_4, allows the identification of the main inflection points that appear in TM-TF plot. These points, corresponding to the main features that exist in the synthetic landform examined, allow the establishment of correlations between filter and landforms. This method offers a more robust tool than the continuous and systematic procedure employed in González-Díez et al. (2021) to extract frequencies. It is therefore unnecessary to use all existing frequencies from the signal to obtain representative FGRs, only the most relevant from this TM-TF plot. FGRs show changes in the general trend of the altimetry, which theoretically helps to objectively identify the main existing geomorphic features, so FGRs and GRs could be equivalent. This equivalence should be sampled when using synthetic models composed of complex morphologies. In this experiment, wherein

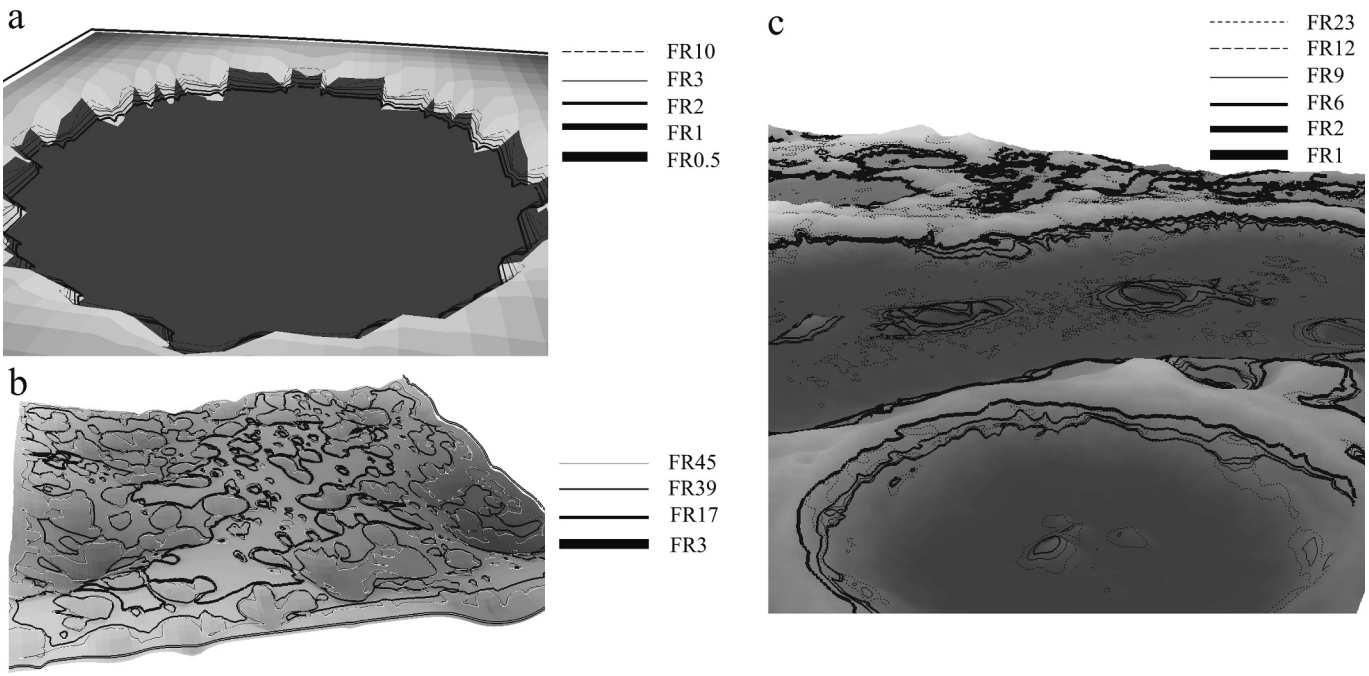

Fig. 10. Three examples of the spatial pattern drawn by the vectors belonging to the respective FGR, in their usage for the identification of real objects. The two first examples belonging to the following SDRM models: (a) flat bottom crater (Experiment_1); (b) a lunar relief emulated (Experiment_2). The third belongs to a real case of the Moon: (c) Mare Ingenii area (Experiment_3). In each example, the spatial pattern of the FGR vectors obtained with its corresponding Filter Radius (FR) are drawn, showing how these vectors border the object silhouette and how they match the real forms present in the DEMs. In the background the corresponding DEM projected in 3D is depicted (using the ArcScene tools V10.8.1).

a simple crater was simulated by script_1, the upper border of the depression (ring-edge) constitutes the GR. The objective limits obtained after analysis of the shape created by a single crater show the ability of the method to obtain the shape limits. Thus, the filter boundaries move towards the ring-edge as the COF increases, reaching a real frequency of 10 (FR10), beyond which the boundary is over-passed. Over this frequency (at COFs 12 and 26), true frequencies are equal or below the sample frequency, thus the Nyquist theorem is in conflict and many Gibbs effect vectors appear on the surface. Therefore, over the second half of the sample frequency (10 and higher TFs), it would be inappropriate to select COF for crater location. Hence, these COF limits are not considered in the following analysis. The repeatability of the spatial distribution of filters employed indicates that the shape analysed is constant in all of them and not an artefact similar to those created by Gibbs-type effects. This spatial repeatability can be used as a cartographic criterion in the identification of crater shapes.

Results provided in Experiment_1 show that the HPF-FFT method offers FGRs that allow the analysis of the correspondence between the filter and the synthetic landform selected, which represents the Moon's most common geomorphic features (Robbins, 2019). In addition, most of the remote sensing methods for detecting craters have been applied to simple crater shapes, considering either flat-bottomed or bowl shapes, with or without raised rims (Martins et al., 2009; Salamunićcar et al., 2014; Stepinski et al., 2012; Barlow, 2015; Scaioni et al., 2018; Yang et al., 2020; Zhou et al., 2020).

4.2. Discussion, Experiment_2

The experiment demonstrated the usefulness of the GUI (script_2) in geomorphological analysis, and its adaptability in generating SDRMs of bowl shapes and different sizes, in agreement with other remote sensing methods. However, modelling more complex reliefs will require scripts that incorporate intricate functions. It also opens the door to include routines that show the evolution of the relief, in the same way as models of wave propagation in a pond, which will make it possible to model the evolution over time of any complex geomorphic feature. Using these models, it is possible to objectively evaluate the FGRs provided by HPF-FFT (including the one used in script_5, or the wide diversity of transfer functions present in the literature) and compare it with the shape provided by the GT, making it possible to establish direct filter-form relationships. The first part of Experiment_2 demonstrates how filters can detect crater-shaped depression boundaries. The smaller the crater, the better the filter detects its boundary, which is not the case for medium-large craters, probably because their boundaries are more diffuse, and the uncertainty of detection occupies spatially a larger area. This means that the confidence in the filter increases with the FR. In the second part of the experiment, in which a simulated lunar relief is obtained by the aggregation of craters of different sizes, crater boundaries become more identifiable as the crater becomes smaller. Even though the crater accretion operation mentioned has erased the footprint of some of the smaller craters. Blurring is noticeable when large and small shapes are in proximity to each other. In those cases, large craters are modified by the many small ones that appear inside them and have a blurred shape merged with smaller ones, as mentioned in other geomorphic contexts (Gorum et al., 2008; Wheaton et al., 2015). However, segmentation procedures could help to isolate them to generate isolated crater inventories. The indicators show that there is still coherence between the FGR and the form.

4.3. Discussion, Experiment_3

The different FRs obtained show their usefulness to characterise different relief units, according to their size of representation within the DEM. Thus, FR1 shows their usefulness in delineating the frontiers between depressions and uplands (Fig. 9b). Up to FR6, many of the large depressions identified by Fortezzo et al. (2020) have been detected (Fig. 9c). If the polygons of all filters (FR1 to FR43) are included, the tool can identify small upland depressions (Fig. 9b-g). However, by selecting FR43 exclusively, the most relevant intra-maria depressions are distinguished (Fig. 9g). As the filter affects higher frequencies, more elements

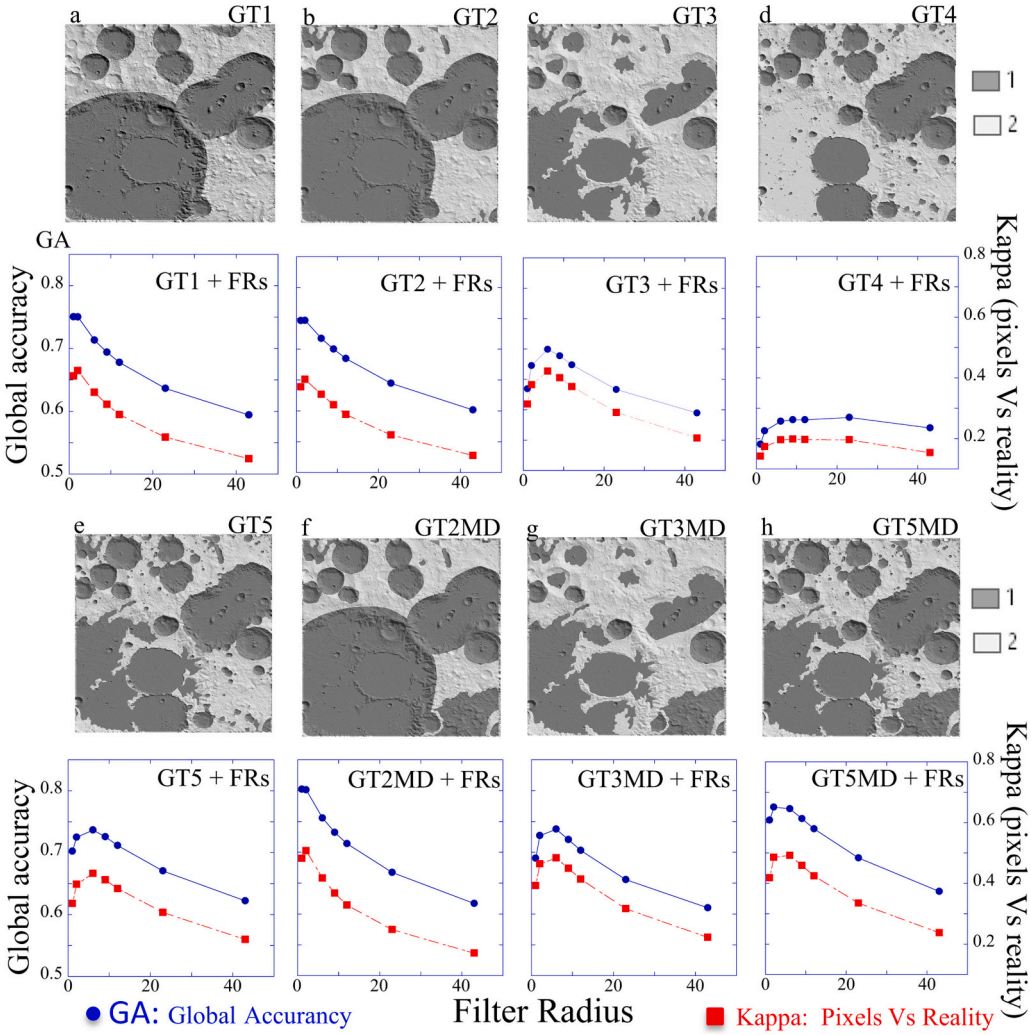

Fig. 11. Results of the combinations carried out in Experiment_3 (Mare Ingenii), between the different filtered DEMs and Ground truth (GT). Upper top, presentation of the following four GTs: (a) GT1; (b) GT2; (c) GT3; (d) GT4. Lower top: cross validation results of the above combinations performed between GT and Filtered SDRMs and their respective accuracy indicators. Upper bottom: presentation of the following four GTs: (e) GT5; (f) GT2MD; (g) GT3MD; (h) GT5MD. Lower bottom, c, cross validation results of the above combinations performed between GT and Filtered SDRMs and their respective accuracy indicators. GT pixels valued as 1 correspond to crater while pixels valued as 2 correspond to no crater. The filtered DEMs correspond to the respective Filter Radius (FR) presented in Fig. 8.

of the dwarf class appear. As shown in Table 6b, the number of polygons increases with FR, creating difficulties in the classification despite the assistance provided by the shaded relief model. The spatial distribution of filtering vectors is an excellent criterion for identifying real relief objects, such as crater shape depressions or uplands, as shown in Fig. 10. In all cases, FGRs delimit the object silhouette. Filtering also shows its ability to delineate relief elements of varying detail. It is striking that there are very few examples of vectors classified as dwarf that spatially coincide with relief elements. Actual dwarves present a clear correspondence with features detectable in the DEM; the rest may be because of small altimetric differences highlighted by the filtering. For this reason, in some subsequent evaluations, this third class was added to the non-crater class to simplify the analysis. The correspondence between FGR and GT presented in (Fig. 11a-b), shows how FR1 provides the best fit, for these types of truths, created from single large, simplified features. Using contacts extracted from GeoUnits provides the best GA and Kappa values when adopting FR6 (Fig. 11c). However, these results are inferior to those previously presented. Despite the work conducted mapping individual craters, GA and Kappa values provided worse results than the previous GTs (Fig. 11d). Once more, the best values are obtained with FR6, but in this case, Kappa reduces notably compared to the former. The combination of contacts from ad hoc craters with GeoUnits produces an improvement in the accuracy results (Fig. 11e). Again, FR6 offers the best results, highlighting a notable increment in Kappa. The next three combinations (Fig. 11f-h) generated, including a deliberated change of the cratered area, offer greater accuracy values in regards previous GTs. Thus, GA is 74.6 % in Fig. 11b, whereas it passes 80 % in Fig. 11f. Again, GA is close to 70 % in Fig. 11c, and >73 % in Fig. 11g. Finally, GA passes from 73 % in Fig. 11e to 77 % in Fig. 11h. Those models that were constructed employing geomorphic indicators, such as Fig. 11f and Fig. 11h, offer the best accuracy results (for GA 80 and 77 %, for Kappa 0.48 and 0.49, respectively). The first has the highest accuracy indicators using FR1, whereas the second uses FR6, probably because it contains smaller features. In any case, both give the highest values of all the accuracy results obtained. Therefore, the closer the GT to reality, the better accuracy values offered. The filter can assess the GT and detect the true reality mapped using it.

Regarding the evaluation of the centroids of the ad hoc inventory, FGRs offer less satisfactory results for GA and Kappa values compared to previous experiments performed in the individual-by-individual test. This could be due to two reasons: the tiny size of many of these geomorphic features; and to the fact that the spatial check is based on a binomial (cratered-not cratered area) established in terms of surface extent.

Finally, the moonscape automatically constructed (Fig. 12) exhibits an enormous coincidence with the relief depicted in the lunar geodatabases (as Fig. 2c, for instance), highlighting a wide number of subunits of relief domains, demonstrating its potential usefulness for moonscape characterisation.

Table 7
Experiment_3. Results of the cross validation between Filtered Model (FM) and Ground Truth (GT) in Experiment_3. The filtered models presented are maned using the Filter Radius (FR) employed during filtering. Accuracy indexes in bold.

GT1_FR1		Ground Truth classes			User	
		Depressions	Summits		Accuracy	Error
		1	2	Total		
FR1 classes						
Depressions	100	36,362,586	10,628,554	46,991,140	0.77	*0.23*
Summits	200	5,121,025	11,138,014	16,259,069	0.68	*0.31*
	Total	41,483,641	21,766,568	63,250,209		
Producer	Accuracy	0.88	0.51			
	Error	*0.12*	*0.49*			
Coincidence pixels and reality		Global Accuracy		**0.75**		
		Kappa		**0.08**		

GT1_FR2		Ground Truth classes			User	
		Depressions	Summits		Accuracy	Error
		1	2	Total		
FR2 classes						
Depressions	100	34,999,678	9,293,480	44,293,158	0.79	*0.21*
Summits	200	6,483,963	12,473,088	18,957,051	0.66	*0.34*
	Total	41,483,641	21,766,568	63,250,209		
Producer	Accuracy	0.84	0.57			
	Error	*0.16*	*0.43*			
Coincidence pixels and reality		Global Accuracy		**0.75**		
		Kappa		**0.43**		

GT1_FR6		Ground Truth classes			User	
		Depressions	Summits		Accuracy	Error
		1	2	Total		
FR6 classes						
Depressions	100	36,737,844	9,368,051	42,105,895	0.77	*0.22*
Summits	200	8,745,797	12,398,517	21,144,314	0.58	*0.41*
	Total	41,483,641	21,766,568	63,250,209		
Producer	Accuracy	0.78	0.56			
	Error	*0.21*	*0.43*			
Coincidence pixels and reality		Global Accuracy		**0.71**		
		Kappa		**0.36**		

GT1_FR9		Ground Truth classes			User	
		Depressions	Summits		Accuracy	Error
		1	2	Total		
FR9 classes						
Depressions	100	31,829,154	9,677,075	41,506,229	0.77	*0.23*
Summits	200	9,654,487	12,089,493	21,743,980	0.56	*0.44*
	Total	41,483,641	21,766,568	63,250,209		
Producer	Accuracy	0.77	0.55			
	Error	*0.23*	*0.44*			
Coincidence pixels and reality		Global Accuracy		**0.69**		
		Kappa		**0.32**		

GT1_FR12		Ground Truth classes			User	
		Depressions	Summits		Accuracy	Error
		1	2	Total		
FR12 classes						
Depressions	100	31,138,906	999,792	41,138,698	0.76	*0.24*
Summits	200	10,344,735	11,766,776	22,111,511	0.53	*0.47*
	Total	41,483,641	21,766,568	63,250,209		
Producer	Accuracy	0.75	0.54			
	Error	*0.25*	*0.46*			
Coincidence pixels and reality		Global Accuracy		**0.68**		
		Kappa		**0.29**		

GT1_FR23		Ground Truth classes			User	
		Depressions	Summits		Accuracy	Error
		1	2	Total		
FR23 classes						
Depressions	100	28,707,713	10,184,962	38,892,675	0.74	*0.26*
Summits	200	12,775,928	11,581,606	24,357,534	0.47	*0.52*
	Total	41,483,641	21,766,568	63,250,209		
Producer	Accuracy	0.69	0.53			
	Error	*0.31*	*0.47*			
Coincidence pixels and reality		Global Accuracy		**0.64**		
		Kappa		**0.22**		

GT1_FR43		Ground Truth classes			User	
		Depressions	Summits		Accuracy	Error
		1	2	Total		
FR43 classes						
Depressions	100	26,093,425	10,251,723	36,345,148	0.72	*0.28*
Summits	200	15,390,216	11,514,845	26,905,061	0.43	*0.57*
	Total	41,483,641	21,766,568	63,250,209		
Producer	Accuracy	0.63	0.53			
	Error	*0.37*	*0.47*			
Coincidence pixels and reality		Global Accuracy		**0.59**		
		Kappa		**0.15**		

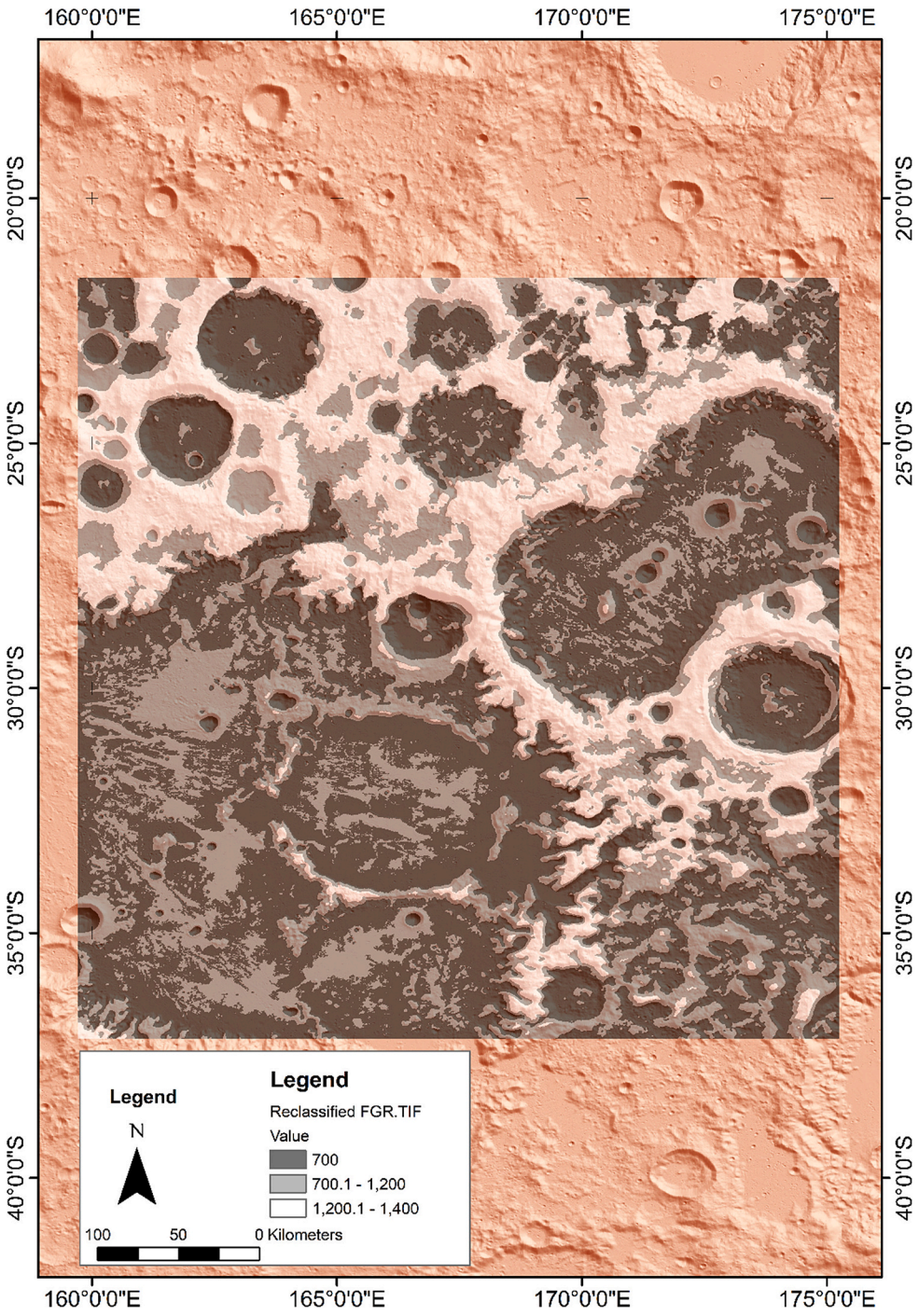

Fig. 12. 3D model for the visualization of the cratered landscape present in Mare Ingenii. The model is created by a combination of the obtained FGRs. Each FGR polygon retains the values assigned (crater, 100; non-crater, 200). The combined model shows units generated by the combination of seven FGRs, returning values ranging from 700 to 1400. These units are grouped in three quantile classes, linearly distributed, showing an objective representation of the three main geomorphic existing units: lowlands (value 700) are maria, large depressions and small crater depression generated by combination of single elements located in low-lying reliefs, etc.; middle lands (values 700.1-1200) are positive reliefs surrounding large depressions, middle slopes, smooth depressions located on high lands; highlands (values 1201-1400) are main ridges including high slopes and all the positive geomorphic features close large depressions, summits, ring of debris at the crater surroundings.

5. Conclusions

The scripts developed for this work have provided flexibility to calculations and for the analysis presented of altimetry variations on planetary surfaces. The packages presented do not substitute the use of professional remote sensing software, but give a different perspective to the problem. Their use has not implied a significant increase of the computing time because most spatial analysis routines are conducted in the GIS. In addition, thanks to these scripts, it has been possible to understand the graphical answer provided by the FFT filters employed. Other didactic advantages are: (i) the great possibilities offered by dozens of free access scripts designed for the analysis of 2D signal using FFT; (ii) illustrative examples on incorporating and visualising the original signal; (iii) processing cases on applying FFTs and its properties; (iv) how to isolate harmonics and subsequently how to represent them. The framework eases the interaction with a pre-designed script, which can be even adapted to the needs of the study performed. There is a sizeable community of researchers who share code for different platforms (Mathworks, GeeksforGeeks, YouTube) with dozens of examples posted, including documentation created by Gonzalez and Woods (2008, 2018).

The scripts presented in this paper have demonstrated their utility, both for the construction of SDRMs and for DEM analysis and filtering. The TM-TF plot provides an efficient way to select the existing sets of frequency within a signal, which can be narrowed down through the minimum frequency criterion. Therefore, using these minima as COFs

offers an objective basis for filter-size selection, enabling a straightforward identification of the main frequencies, equivalent to the studied geomorphic elements.

Using Butterworth transference functions offers a relevant improvement regarding the Gaussians employed in González-Díez et al. (2021). Its design incorporates the possibility of applying either an Ideal or a Gaussian pattern, thanks to the order number included in the function, providing a great versatility of applications in geomorphic studies.

The SDRMs used have shown suitability for the analysis of cratered landforms when applying the present methodology. Either the model that emulates a single flat-bottomed crater or the composite crater model that emulates cratered landscapes, generated by the addition of numerous bowl-shaped craters, enable the HPF analysis. The designed GUI has great utility not only in crater morphologies but also in other positive geo-forms.

In this work, we have carried out several experiments of increasing complexity in order to evaluate the detection of altimetry variations of the lunar surface, due to either bowl-shaped craters or larger mare-infilled basins. The main outcome of Experiment_1 demonstrates a close correspondence between the FGRs obtained by the HPF-FFT method and the synthetic landform selected (flat-bottomed crater). The spatial repetition of the FGRs can be used as a cartographic criterion in the identification of this type of crater-shaped depression. Whereas Experiment_2 shows that in landscapes generated by the addition of geomorphic features of different sizes, the smaller the crater, the better the filters detect its boundaries. This does not occur with medium-large craters because their limits are more diffuse as they were created by adding individual models. Therefore, the rims of small craters are more reliably detected than those of medium-sized craters, which are in turn more faithfully identified than those of the larger impact structures. The confidence in the filter increases with FR. Finally, the blurring effects originate from the presence of smaller craters within larger ones, or through the merging with smaller craters.

The ad hoc crater inventory created in Experiment_3 includes 479 craters with areas ranging from 1 to 28,736 km^2. The application of the TM-TF plot in the DEM area of Mare Ingenii has allowed the identification of 7 sets of dominant frequencies. These provide the selection of seven FGRs that have returned over 21,700 polygons, of which 783 are craters, 2782 non-craters and 18,195 dwarf polygons. Many of these belong to the same landform, although they were identified in different FGRs. The number of polygons detected by filters increases with the FR, introducing difficulties in the classification despite the help provided by the shade model. The spatial distribution of filtering vectors is an excellent criterion for identifying actual relief objects, such as craters or mountains. In addition, this spatial repetition of the FGRs obtained, employing either synthetic or real models, can be used as a criterion to identify the existence of ring-edge features, like those generated by impact craters, or also the base of positive polarity geomorphic features, such as hills. Accuracy indicators (GA and Kappa) show how crater detection success increases as crater size decreases. The GA of each scenario reaches its maximum value with large FRs, improving if the size of the craters decreases. Kappa shows higher confidence with the higher FR filters. The consideration of all individual geomorphic elements is a key point in assessing the accuracy of composite shapes. Thus, the accuracy indicators (GA and Kappa) extracted from the FGR built on the SDRMs generated by crater aggregation show how the detection success increases as smaller craters are aggregated. In addition, the detection success improves slightly as the FR increases. The FGRs obtained from HPS-FFT have the capacity to assess true reality mapped in the GT employed. The proposed accuracy indices could be improved through the use of additional indicators, as suggested by Foody (2020). Either GA or Kappa show a reasonable measure of success by the HPF-FFT to obtain FGRs of relief domains. Finally, the generation of geomorphic units by combining FGRs demonstrates the usefulness of the method for the objective characterisation of the moonscape.

Declaration of competing interest

The authors declare that they have no known competing financial interests or personal relationships that could have appeared to influence the work reported in this paper.

Data availability

Data will be made available on request.

Acknowledgments

This work was carried out as part of the Projects: 29.P114.64004 (UC); 29.P203.64004 (UC); RECORNISA (FLTQ-UC). We thank the reviewers and the editor for their constructive criticisms and suggestions, which helped us to improve the initial version of the manuscript.

Appendix A. Supplementary data

Supplementary data to this article can be found online at https://doi.org/10.1016/j.geomorph.2023.108753.

References

Astropedia, 2021a. Astrogeology_1 [WWW Document]. PDS-NASA-USGS. https://astrogeology.usgs.gov/search?pmi-target=moon. (Accessed 12 December 2021).

Astropedia, 2021b. Astrogeology_2 [WWW Document]. PDS-NASA-USGS. https://astrogeology.usgs.gov/search/details/Moon/LRO/LOLA/Lunar_LRO_LOLA_Global_LDEM_118m_Mar2014/cub. (Accessed 12 December 2021).

Astropedia, 2021c. Astrogeology_3 [WWW Document]. PDS-NASA-USGS. https://astrogeology.usgs.gov/search/map/Moon/Geology/Unified_Geologic_Map_of_the_Moon_GIS_v2. (Accessed 12 December 2021).

Baker, D.M.H., Head, J.W., Collins, G.S., Potter, R.W.K., 2016. The formation of peak-ring basins: Working hypotheses and path forward in using observations to constrain models of impact-basin formation. Icarus 273, 146–163. https://doi.org/10.1016/j.icarus.2015.11.033.

Barlow, N.G., 2015. Constraining geologic properties and processes through the use of impact craters. Geomorphology 240, 18–33. https://doi.org/10.1016/j.geomorph.2014.08.027.

Chappelow, J.E., Sharpton, V.L., 2002. An improved shadow measurement technique for constraining the morphometry of simple impact craters. Meteorit. Planet. Sci. 37, 479–486. https://doi.org/10.1111/j.1945-5100.2002.tb00834.x.

Chin, G., Brylow, S., Foote, M., Garvin, J., Kasper, J., Keller, J., Litvak, M., Mitrofanov, I., Paige, D., Raney, K., Robinson, M., Sanin, A., Smith, D., Spence, H., Spudis, P., Stern, S.A., Zuber, M., 2007. Lunar reconnaissance orbiter overview: the instrument suite and mission. Space Sci. Rev. 129, 391–419. https://doi.org/10.1007/s11214-007-9153-y.

Darishchev, A., Guérillot, D., 2017. Towards Realistic Synthetic Models of Middle East Carbonate Reservoirs for Evaluating Reservoir Engineering Workflows. European Association of Geoscientists & Engineers. https://doi.org/10.3997/2214-4609.201701701 p. cp-519-00051.

Di Fiore, V., 2010. Seismic site amplification induced by topographic irregularity: results of a numerical analysis on 2D synthetic models. Eng. Geol. 114, 109–115. https://doi.org/10.1016/j.enggeo.2010.05.006.

Fisher, P.F., Tate, N.J., 2006. Causes and consequences of error in digital elevation models. Prog. Phys. Geogr. 30, 467–489. https://doi.org/10.1191/0309133306pp492ra.

Foody, G.M., 2020. Explaining the unsuitability of the kappa coefficient in the assessment and comparison of the accuracy of thematic maps obtained by image classification. Remote Sens. Environ. 239, 111630 https://doi.org/10.1016/j.rse.2019.111630.

Fortezzo, C.M., Spudis, P.D., Harrel, S.L., 2020. RELEASE OF THE DIGITAL UNIFIED GLOBAL GEOLOGIC MAP OF THE MOON AT 1:5,000,000- SCALE, in: 51st Lunar and Planetary Science Conference.

Garbrecht, J., Martz, L.W., 1999. Digital Elevation Model Issues in Water Resources. Modeling. In1999 ESRI Users Conf. Proceedings. Eletronic Doc. In: https://gis.esri.com/library/userconf/proc99/proceed/papers/pap866/p866.htm.

Geeksforgeeks, 2021. MATLAB – Butterworth highpass filter in image processing [WWW Document]. In: https://www.geeksforgeeks.org/matlab-butterworth-highpass-filter-in-image-processing/. (Accessed 2 November 2021).

Gonzalez, R.C., Woods, R.E., 2008. Digital Image Processing Third Edition Pearson 1–076.

Gonzalez, R.C., Woods, R.E., 2018. Digital image processing, 4TH. EDITION Pearson.

Gonzalez, R.C., Woods, R.E., Eddins, S.L., 2009. Digital Image Processing Using MATLAB®, Second Edi. ed. Gatesmark Publishing.

González-Díez, A., Barreda-Argüeso, J.A., Rodríguez-Rodríguez, L., Fernández-Lozano, J., 2021. The use of filters based on the Fast Fourier Transform applied to DEMs for the objective mapping of karstic features. Geomorphology 385, 107724. https://doi.org/10.1016/j.geomorph.2021.107724.

González-Díez, A., Barreda-Argüeso, J.A., Rodríguez-Rodríguez, L., Riquelme, A., 2022a. adririquelme/Single Crater Generator script. [WWW Document]. URL. https://github.com/adririquelme/singlecratergenerator. (Accessed 21 March 2022).
González-Díez, A., Barreda-Argüeso, J.A., Rodríguez-Rodríguez, L., Riquelme, A., 2022b. Adririquelme/DEM_kernel_generator: DEM of kernels for volcanos or craters. [WWW Document]. URL. https://github.com/adririquelme/DEM_kernel_generator. (Accessed 21 March 2022).
Gorum, T., Gonencgil, B., Gokceoglu, C., Nefeslioglu, H.A., 2008. Implementation of reconstructed geomorphologic units in landslide susceptibility mapping: the Melen Gorge (NW Turkey). Nat. Hazards 46, 323–351. https://doi.org/10.1007/s11069-007-9190-6.
Grumpe, A., Belkhir, F., Wöhler, C., 2014. Construction of lunar DEMs based on reflectance modelling. Adv. Sp. Res. 53, 1735–1767. https://doi.org/10.1016/j.asr.2013.09.036.
Guth, P.L., Van Niekerk, A., Grohmann, C.H., Muller, J.P., Hawker, L., Florinsky, I.V., Gesch, D., Reuter, H.I., Herrera-Cruz, V., Riazanoff, S., López-Vázquez, C., Carabajal, C.C., Albinet, C., Strobl, P., 2021. Digital elevation models: terminology and definitions. Remote Sens. 13, 1–19. https://doi.org/10.3390/rs13183581.
Haruyama, J., Matsunaga, T., Ohtake, M., Morota, T., Honda, C., Yokota, Y., Torii, M., Ogawa, Y., 2008. Global lunar-surface mapping experiment using the Lunar imager/spectrometer on SELENE. Earth, Planets Sp. 60, 243–255. https://doi.org/10.1186/BF03352788.
He, S., Cai, H., Liu, S., Xie, J., Hu, X., 2021. Recovering 3D basement relief using gravity data through convolutional neural networks. J. Geophys. Res. Solid Earth 126, 1–30. https://doi.org/10.1029/2021JB022611.
Head, J.W., Fassett, C.I., Kadish, S.J., Smith, D.E., Zuber, M.T., Neumann, G.A., Mazarico, E., 2010. Global distribution of large lunar craters: implications for resurfacing and impactor populations. Science 329, 1504–1507. https://doi.org/10.1126/science.1195050.
Hesse, R., 2010. LiDAR-derived local relief models - a new tool for archaeological prospection. Archaeol. Prospect. 17, 67–72. https://doi.org/10.1002/arp.374.
Hiesinger, H., Head .I.I.I., James W., 2006. New views of lunar geoscience: an introduction and overview. Rev. Mineral. Geochem. 60, 1–81. https://doi.org/10.2138/rmg.2006.60.1.
Irg1994, 2012. Matlab Ecuacion de ondas [WWW Document]. La web Física. URL. https://forum.lawebdefisica.com/forum/el-aula/métodos-informáticos/24017-ecuacion-de-ondas. (Accessed 14 November 2021).
Kasai, M., Ikeda, M., Asahina, T., Fujisawa, K., 2009. LiDAR-derived DEM evaluation of deep-seated landslides in a steep and rocky region of Japan. Geomorphology 113, 57–69. https://doi.org/10.1016/j.geomorph.2009.06.004.
Kato, M., Takizawa, Y., Sasaki, S., et al., 2006. Selene, the Japanese lunar orbiting satellites mission: present status and science goals. In: 37th Annual Lunar and Planetary Science Conference, p. 1233.
Keaton, J., Haneberg, W.C., 2013. Landslide hazard inventories and uncertainty associated with ground truth. In: Faquan, W., Qi, S. (Eds.), Global View of Engineering Geology and the Environment. Taylor and Francis Group, London, pp. 105–110.
Lampert, T.A., Stumpf, A., Gançarski, P., 2016. An empirical study into annotator agreement, ground truth estimation, and algorithm evaluation. IEEE Trans. Image Process. 25, 2557–2572. https://doi.org/10.1109/TIP.2016.2544703.
Liu, X., 2008. Airborne LiDAR for DEM generation: some critical issues. Prog. Phys. Geogr. 32, 31–49. https://doi.org/10.1177/0309133308089496.
Lloyd, C.D., Atkinson, P.M., 2006. Deriving ground surface digital elevation models from LiDAR data with geostatistics. Int. J. Geogr. Inf. Sci. 20, 535–563. https://doi.org/10.1080/13658810600607337.
Lohani, B., Ghosh, S., 2017. Airborne LiDAR technology: a review of data collection and processing systems. Proc. Natl. Acad. Sci. India Sect. A - Phys. Sci. 87, 567–579. https://doi.org/10.1007/s40010-017-0435-9.
Martins, R., Pina, P., Marques, J.S., Silveira, M., 2009. Crater detection by a boosting approach. IEEE Geosci. Remote Sens. Lett. 6, 127–131. https://doi.org/10.1109/LGRS.2008.2006004.
Matsunaga, T., Ohtake, M., Haruyama, J., Ogawa, Y., Nakamura, R., Yokota, Y., Morota, T., Honda, C., Torii, M., Abe, M., Nimura, T., Hiroi, T., Arai, T., Saiki, K., Takeda, H., Hirata, N., Kodama, S., Sugihara, T., Demura, H., Asada, N., Terazono, J., Otake, H., 2008. Discoveries on the lithology of lunar crater central peaks by SELENE spectral profiler. Geophys. Res. Lett. 35, 6–7. https://doi.org/10.1029/2008GL035868.
Mazarico, E., Rowlands, D.D., Neumann, G.A., Smith, D.E., Torrence, M.H., Lemoine, F.G., Zuber, M.T., 2012. Orbit determination of the lunar reconnaissance orbiter. J. Geod. 86, 193–207. https://doi.org/10.1007/s00190-011-0509-4.
Melosh, H.J., 1989. Impact Cratering: A Geologic Process. New York Oxford Univ. Press. Oxford Clarendon Press.
Neumann, G.A., Smith, D.E., Scott, S.R., Slavney, S., Grayzek, E., 2011. Lunar Reconnaissance Orbiter Lunar Orbiter Laser Altimeter reduced data record and derived products software interface specification, version 2.42, National Aeronautics and Space Administration Planetary Data System. https://lunar.gsfc.nasa.gov/lola/images/LOLA_RDRSIS.pdf. (Accessed 20 August 2021).
Neumann, G.A., Zuber, M.T., Wieczorek, M.A., Head, J.W., Baker, D.M.H., Solomon, S.C., Smith, D.E., Lemoine, F.G., Mazarico, E., Sabaka, T.J., Goossens, S.J., Melosh, H.J., Phillips, R.J., Asmar, S.W., Konopliv, A.S., Williams, J.G., Sori, M.M., Soderblom, J.M., Miljkovic, K., Andrews-Hanna, J.C., Nimmo, F., Kiefer, W.S., 2015. Planetary science: lunar impact basins revealed by gravity recovery and interior laboratory measurements. Sci. Adv. 1, 1–11. https://doi.org/10.1126/sciadv.1500852.
Ohtake, M., Haruyama, J., Matsunaga, T., Yokota, Y., Morota, T., Honda, C., Team, L., 2008. Performance and scientific objectives of the SELENE (KAGUYA) Multiband Imager. Earth Planet. Space. 60, 257–264. https://doi.org/10.1186/BF03352789.
Povilaitis, R.Z., Robinson, M.S., van der Bogert, C.H., Hiesinger, H., Meyer, H.M., Ostrach, L.R., 2018. Crater density differences: exploring regional resurfacing, secondary crater populations, and crater saturation equilibrium on the moon. Planet. Space Sci. https://doi.org/10.1016/j.pss.2017.05.006.
Regina, U., 2021. CS425 Lab: Frequency Domain Processing [WWW Document]. https://www.studocu.com/en-us/document/university-of-washington/electromagnetics-ii/2d-fft/4450616. (Accessed 20 August 2021).
Robbins, S.J., 2019. A new global database of lunar impact craters >1–2 km: 1. Crater locations and sizes, comparisons with published databases, and global analysis. J. Geophys. Res. Planets 124, 871–892. https://doi.org/10.1029/2018JE005592.
Robinson, M.S., Brylow, S.M., Tschimmel, M., Humm, D., Lawrence, S.J., Thomas, P.C., Denevi, B.W., Bowman-Cisneros, E., Zerr, J., Ravine, M.A., Caplinger, M.A., Ghaemi, F.T., Schaffner, J.A., Malin, M.C., Mahanti, P., Bartels, A., Anderson, J., Tran, T.N., Eliason, E.M., McEwen, A.S., Turtle, E., Jolliff, B.L., Hiesinger, H., 2010. Lunar reconnaissance orbiter camera (LROC) instrument overview. Space Sci. Rev. 150, 81–124. https://doi.org/10.1007/s11214-010-9634-2.
Salamunićcar, G., Lončarić, S., Grumpe, A., Wöhler, C., 2014. Hybrid method for crater detection based on topography reconstruction from optical images and the new LU78287GT catalogue of Lunar impact craters. Adv. Sp. Res. 53, 1783–1797. https://doi.org/10.1016/j.asr.2013.06.024.
Scaioni, M., Yordanov, V., Brunetti, M.T., Melis, M.T., Zinzi, A., Kang, Z., Giommi, P., 2018. Recognition of landslides in lunar impact craters. Eur. J. Remote Sens. 51, 47–61. https://doi.org/10.1080/22797254.2017.1401908.
Smith, D., Zuber, M., Neumann, G.~.A., Mazarico, E., Head, J., Torrence, M.~.H., Lola Science Team, 2011. results from the lunar orbiter laser altimeter (lola): global, high resolution topographic mapping of the moon. In: 42nd Annual Lunar and Planetary Science Conference, p. 2350.
Stepinski, T.F., Ding, W., Vilalta, R., 2012. Detecting impact craters in planetary images using machine learning. In: Magdalena-Benedito, R., Martínez-Sober, M., Martínez-Martínez, J.M., Vila-Francés, J., Escadell-Montero, P. (Eds.), Intelligent Data Analysis for Real-Life Applications: Theory and Practice, IGI Global. https://doi.org/10.4018/978-1-4666-1806-0.ch008.
Thelin, G.P., Pike, R.J., 1991. Landforms of the conterminous United States: a digital shaded-relief portrayal. US Geol. Surv. https://doi.org/10.3133/i2206.
Tooley, C.R., Houghton, M.B., Saylor, R.S., Peddie, C., Everett, D.F., Baker, C.L., Safdie, K.N., 2010. Lunar reconnaissance orbiter mission and spacecraft design. Space Sci. Rev. 150, 23–62. https://doi.org/10.1007/s11214-009-9624-4.
Wang, J., Cheng, W., Zhou, C., 2015. A Chang'E-1 global catalog of lunar impact craters. Planet. Space Sci. 112, 42–45. https://doi.org/10.1016/j.pss.2015.04.012.
Weiss, A.D., 2001. Topographic position and landforms analysis. In: Poster Present. ESRI User Conf. San Diego, CA, 64, pp. 227–245.
Werbrouck, I., Antrop, M., Van Eetvelde, V., Stal, C., De Maeyer, P., Bats, M., Bourgeois, J., Court-Picon, M., Crombé, P., De Reu, J., De Smedt, P., Finke, P.A., Van Meirvenne, M., Verniers, J., Zwertvaegher, A., 2011. Digital Elevation Model generation for historical landscape analysis based on LiDAR data, a case study in Flanders (Belgium). Expert Syst. Appl. 38, 8178–8185. https://doi.org/10.1016/j.eswa.2010.12.162.
Wheaton, J.M., Fryirs, K.A., Brierley, G., Bangen, S.G., Bouwes, N., O'Brien, G., 2015. Geomorphic mapping and taxonomy of fluvial landforms. Geomorphology 248, 273–295. https://doi.org/10.1016/j.geomorph.2015.07.010.
Yang, C., Zhao, H., Bruzzone, L., Benediktsson, J.A., Liang, Y., Liu, B., Zeng, X., Guan, R., Li, C., Ouyang, Z., 2020. Lunar impact crater identification and age estimation with Chang'E data by deep and transfer learning. Nat. Commun. 11, 1–15. https://doi.org/10.1038/s41467-020-20215-y.
Yokoyama, R., Shirasawa, M., Pike, R.J., 2002. Visualizing topography by openness: a new application of image processing to digital elevation models. Photogramm. Eng. Remote Sens. 68, 257–265.
Zhou, X., Xie, X., Xue, Y., Xue, B., Qin, K., Dai, W., 2020. Bag of geomorphological words: a framework for integrating terrain features and semantics to support landform object recognition from high-resolution digital elevation models. ISPRS Int. J. Geo-Inf. 9, 1–18. https://doi.org/10.3390/ijgi9110620.